Title
Properties of adsorbates in III-V semiconductors

Permalink
https://escholarship.org/uc/item/5kp4060h

Author
Winn, Darby L.

Publication Date
2007

Peer reviewed|Thesis/dissertation

UNIVERSITY OF CALIFORNIA, SAN DIEGO

PROPERTIES OF ADSORBATES
ON III-V SEMICONDUTORS

A dissertation submitted in partial satisfaction of the

requirements for the degree Doctor of Philosophy

in

Chemistry

by

Darby L. Winn

Committee in charge:

Professor Andrew C. Kummel, Chair
Professor David N. Hendrickson
Professor Amitabha Sinha
Professor John H. Weare
Professor Edward T. Yu

2007

The dissertation of Darby L. Winn is approved, and it is acceptable in quality and form for publication on microfilm:

_____

_____

_____

_____

_____

Chair

UNIVERSITY OF CALIFORNIA, SAN DIEGO

2007

DEDICATION

This thesis is dedicated to my Dad (Will Winn), Mom (Nancy Winn) and Alex Feldman without whose support this would never have been possible.

TABLE OF CONTENTS

LIST OF SYMBOLS AND ABBREVIATIONS

Aluminum	Al
Angstrom	Å
Arsenic	As
Auger Electron Spectroscopy	AES
Capacitance Voltage	CV
Celsius	C
Centimeter	cm
Chlorine	Cl
Current	I
Degree	º
Density Functional Theory	DFT
Density of States	DOS
Electron	e^-
Electron Volt	eV
Enthalpy of Adsorption	ΔH
Et Alia	*et al.*
Gadolinium	Gd
Gallium	Ga
Germanium	Ge
Germanium on Insulator	GOI
Hour	h
Hydrogen	H
Indium	In
Low Energy Electron Diffraction	LEED
Metal Oxide Field Effect Transistor	MOSFET
Minute	min
Monolayer	ML
Nanoampere	nA
Nanometer	nm
Nitrogen	N
Oxygen	O
Perdew-Burke-Ernzerhof	PBE
Perdew-Wang 1991	PW91
Phosphorus	P
Projected Density of States	PDOS
Projector Augmented Wave	PAW
Sample Voltage	V_s
Second	s

Silicon	Si
Scanning Tunneling Microscopy	STM
Scanning Tunneling Spectroscopy	STS
Tunneling Current	I_t
Ultra High Vacuum	UHV
Vienna *ab initio* Simulation Package	VASP
Versus	vs.
Volt	V

LIST OF FIGURES

Chapter One Figures

Chapter Two Figures

Chapter Three Figures

Chapter Four Figures

LIST OF TABLES

Chapter One Tables

Chapter Four Table

PREFACE

Over the last three decades many attempts mostly unsuccessful, have been made to construct a III-V metal oxide semiconductor field effect transistors (MOSFET) devices.[1-10] The potential advantages of these devices include lower power consumption and higher gain than commercially available Si MOSFETs. Three appropriate channel materials for these devices are GaAs, InAs, and InGaAs. When constructing a Si MOSFET device, Si is exposed to an oxidizing atmosphere (O, O_2, O_3, and H_2O) and the resulting oxide, SiO_2, leaves the Fermi level unpinned.[11] However, when GaAs, InAs, or InGaAs are exposed to the same oxidizing agents bands bend, pinning the Fermi level, which makes the device inoperable.[12,13] Therefore, it becomes necessary to find a new oxide for each material that leaves the Fermi level unpinned. An in depth understanding of the oxide pinning mechanisms on III-V semiconductors can help identify appropriate oxides for other III-V semiconductors. To fully understand the oxide/semiconductor interface an atomistic understanding of both the surface reconstruction of the semiconductor and the semiconductor/oxide interface are needed.

Chapter one presents an in depth study of the correlation between atomic bonding sites and the electronic structure of molecular SiO on GaAs(001)-$c(2\times8)/(2\times4)$. In this study, detailed scanning tunneling microscopy (STM) images and scanning tunneling spectroscopy (STS) spectra are presented. STM images reveal

six different SiO bonding geometries. In addition, the STS spectra show that the Fermi level is pinned midgap at ~5% monolayer (ML) coverage. Density functional theory (DFT) calculations confirmed the experimental findings and helped elucidate the causes of the Fermi level pinning. The Fermi level pinning was found to have either a direct (local charge buildup, and/or partially-filled dangling bonds on Si atoms) or indirect (undimerized surface As atoms) mechanism.

Chapter two compares and contrasts the electronic effects of a wide range of adsorbates on GaAs(001)-c(2×8)/(2×4), including O_2, In_2O, Ga_2O, and SiO. STS measurements revealed that the only adsorbate that left the Fermi level unpinned was Ga_2O. DFT calculations were employed to help deduce the cause of the Fermi level pinning observed for the other three adsorbates. Two distinct pinning mechanisms were found: direct and indirect Fermi level pinning. O_2 was found to pin the Fermi level indirectly on GaAs(001)-c(2×8)/(2×4), while In_2O was found to pin the Fermi level directly. In the case of SiO chemisorbed to GaAs(001)-c(2×8)/(2×4) both pinning mechanisms were present.

The electron mobility of InAs is ~3.8 times greater than GaAs, making it a more promising material than GaAs for a high gain MOSFET device.[14] However, there are very few publications showing an atomic understanding of InAs; even the InAs surface reconstructions are not well understood. Therefore, before attempts can be made to understand the interactions between adsorbates and the InAs surface it is necessary to identify the InAs(001)-(4×2) surface reconstruction. Chapter three

focuses on this task.   Detailed STM images, along with DFT calculations, identified the InAs(001)-(4×2) reconstruction as the undimerized β3(4×2) reconstruction.

Although the electron mobility of InAs is ~3.8 times greater than GaAs, the band gap of InAs is only 0.36 eV, causing a significant number of electrons to be promoted from the valence band maximum to the conduction band at room temperature.[15]   Although this device would be higher gain than a GaAs device it would also have higher standby power, which is not always desirable. Combining InAs and GaAs gives a material with a higher mobility than GaAs but a larger band gap than InAs, enabling a low power high gain device to be constructed. Chapter four outlines a computational study of In_2O and Ga_2O bonding to $In_{.37}Ga_{.63}As(001)$-(2×4). The results show that In_2O and Ga_2O bonding to $In_{0.37}Ga_{0.63}As(001)$-(2×4) is similar to In_2O and Ga_2O bonding to GaAs(001)-(2×4). However, some substantial differences exist between the two systems. The most significant difference between the two systems is that it takes more adsorbates bonded in close proximity before states are induced at the band gap edges for $In_{0.37}Ga_{0.63}As(001)$-(2×4) than for GaAs(001)-(2×4). This difference is attributed to the fact that $In_{0.37}Ga_{0.63}As(001)$-(2×4) has a smaller band gap than GaAs(001)-(2×4).

ACKNOWLEDGEMENTS

Throughout my PhD program I have been surrounded by individuals who have helped me to progress in my program. Without their help this would not have been possible.

I would like to thank Andy Kummel and the past and present members of the Kummel lab for their enlightening scientific discussions and their encouragements. I especially want to thank all of the people who have helped keep Spud (the UHV chamber) up and running and producing data: Mike Hale, Nancy Santagata, and Jian Shen. In addition, I want to thank Tyler Grassman for helping me learn DFT computational techniques and being patient during the entire process.

Outside of work I also have a strong support group of family and friends that I would like to acknowledge. I would like to thank my Dad for giving me the love for science that got me here. In addition, I would like to thank my Mom for her encouragement and support. Lastly, I would like to thank Alex Feldman who spent many hours proofreading papers, listing to upcoming presentations, and giving me an extra hand when I needed it.

This dissertation contains in part or in full, the following publication which have been accepted for publication:

D.L. Winn, M.J. Hale, T.J. Grassman, A.C. Kummel, R. Droopad, and M. Passlack "Direct and Indirect Causes of Fermi Level Pinning at the SiO/GaAs Interface," *The Journal of Chemical Physics* **126** (8) (2007). Chapter 1

This dissertation contains in part or in full, the following publications which have been submitted or are in final preparation for publication:

D.L. Winn, M.J. Hale, T.J. Grassman, J.Z. Sexton, A.C. Kummel, M. Passlack, and R. Droopad "Electronic Properties of Adsorbates on GaAs(001)-c(2×8)/(2×4)," Submitted to *The Journal of Chemical Physics.* Chapter 2

D.L. Winn, J. Shen, J.B. Clemens, T.J. Grassman, A.C. Kummel, R. Droopad, and M. Passlack "Definitive Identification of the InAs(001)-c(8×2)/(4×2) Reconstruction" In preparation for submission to *Surface Science.* Chapter 3

D.L. Winn, T.J Grassman, and A.C. Kummel "Electronic Properties of Adsorbates on In$_{0.37}$Ga$_{0.63}$As(001)-(2×4)," In preparation for submission to *ECS Transactions.* Chapter 4

VITA

Born
Santa Barbara, California   1978

Education
Ph.D., Chemistry
University of California, San Diego   2003-2007
M.S. Chemistry
University of California, San Diego   2001-2003
B.S., Chemistry and Physics
University of California, Santa Barbara   1997-2001

Teaching Experience
Teaching Assistant University of California, San Diego
Physical Chemistry Laboratory (105 A/B)   Spring 2002
Physical Chemistry Laboratory (105 A/B)   Winter 2002
Physical Chemistry (131 A)   Fall 2001

Honors and Awards
Young Scientist Award (PCSI)   2007
Teaching Assistant Excellence Award   2002
Willard L McRary Prize in Chemistry   2001

Presentations
1. Physics and Chemistry of Semiconductor Interfaces (poster 2007): "STM and DFT Determination of the InAs(001)-(4×2) Structure"
2. American Vacuum Society (poster 2006): "Electronic Properties of Adsorbates on GaAs(001)-c(2×8)/(2×4)"
3. Physics and Chemistry of Semiconductor Interfaces (poster 2006): "SiO/GaAs Charge Buildup Induced Pinning"
4. American Vacuum Society (oral 2005): "SiO/GaAs Charge Buildup Induced Pinning"
5. America Vacuum Society (oral 2004): "An atomic understanding of the sub-monolayer interface formed upon the deposition of SiO on GaAs(001)-c(2×8)/(2×4)"
6. The Physics and Chemistry of Semiconductor Interfaces (poster 2004): "Fermi Level Pinning and Unpinning of GaAs(001)-c(2×8)/(2×4) by SiO and Ga_2O: The Role of Surface Charge"

7. American Vacuum Society / Southern California American Vacuum Society Leading Edge Symposium (oral 2003): "Understanding Fermi Level Pinning of SiO on GaAs(001)-(2×4)"
8. The Physics and Chemistry of Semiconductor Interfaces (poster 2003): "Understanding Fermi Level Pinning of SiO on GaAs(001)-(2×4)"
9. Southern California American Vacuum Society Leading Edge Symposium (poster 2002): "Understand Fermi Level Pinning of SiO on GaAs(001)-(2×4)
10. American Chemical Society (poster 2000): "Preparation and Characterization of Molecular Semiconductor Thin Films"

Publications

1. D.L. Winn, J. Shen, J.B. Clemens, T.J. Grassman, and A.C. Kummel "Definitive Identification of the InAs(001)-c(8×2)/(4×2) Reconstruction" In preparation for submission to *Surface Science.*
2. D.L. Winn, T.J. Grassman, and A.C. Kummel "Electronic Properties of Adsorbates on In$_{0.37}$Ga$_{0.63}$As(001)-(2×4)" In preparation for submission to *ECS Transactions.*
3. D.L. Winn, M.J. Hale, T.J. Grassman, J.Z. Sexton, A.C. Kummel, R. Droopad, and M. Passlack "Electronic Properties of Adsorbates on GaAs(001)-c(2×8)/(2×4)" Submitted to *J. Chem. Phys.*
4. D.L. Winn, M.J. Hale, T.J. Grassman, A.C. Kummel, R. Droopad, and M. Passlack "Direct and Indirect Causes of Fermi Level Pinning at the SiO/GaAs Interface," *J. Chem. Phys.* 126,(8): 084703 (Feb 28 2007).
5. M.J. Hale, D.L. Winn, T.J. Grassman, A.C. Kummel, R. Droopad "Chemical Resolved Scanning Tunneling Microscopy Imaging of Al on *p*-type Al$_{0.1}$Ga$_{0.9}$As(001)-c(2×8)/(2×4)," *J. Chem. Phys.* 122,(12): 124702 (Mar 22 2005).
6. M.J. Hale, J.Z. Sexton, D.L. Winn, M. Passlack, and A.C. Kummel "The Influence of Bond Flexibility and Molecular Size on the Chemically Selective Bonding of In$_2$O and Ga$_2$O on GaAs(001)-c(2×8)/(2×4)," *J. Chem. Phys.* 120, (12): 5745-5754 (MAR 22 2004).
7. G.M. Credo, P.J. Carson, D.L. Winn, and S.K. Buratto, "Nanoscale Photophysics of Alq(3) Films," *Synthetic Met.* 121 (1-3): 1393-1394 (March 15 2001).
8. G.M. Credo, D.L. Winn and S.K. Buratto, "Near-Field Scanning Optical Microscopy of Temperature-and Thickness-Dependent Morphology and Fluorescence in Alq(3) Films," *Chem. Mater* 13 (4): 1258-1265 (April 2001).
9. G.M. Credo, G.M. Lowman, J.A. DeAro, P.J. Carson, D.L. Winn and S.K. Buratto, "Probing Nanoscale Photo-Oxidation in Organic Films Using Spatial Hole Burning Near-Field Scanning Optical Microscopy," *J. Chem. Phys.* 112 (18): 7864-7872 (May 2000).

Field of Study

Major Field: Chemistry (Physical Chemistry)
Studies in Surface Science
Professor Andrew Kummel

Major Field: Chemistry (Physical Chemistry)
Studies in Surface Science
Professor Steven Buratto

ABSTRACT OF THE DISSERTATION

PROPERTIES OF ADSORBATED
ON III-V SEMICONDUCTORS

by

Darby L. Winn

Doctor of Philosophy in Chemistry

University of California, San Diego, 2007

Professor Andrew Kummel, Chair

In order to develop a III-V MOSFET device it is important to have an atomic

understanding of both the clean III-V surface reconstruction and the interface formed

when an adsorbate is deposited onto the surface. Three promising channel materials

for a III-V MOSFET devices are GaAs, InAs, and InGaAs. In an effort to obtain an

atomic understanding of the III-V materials and the interfaces that form when

adsorbates bond to them, three critical techniques [scanning tunneling microscopy

(STM), scanning tunneling spectroscopy (STS), and density functional theory (DFT)]

were employed. STM was used to characterize the adsorbate/semiconductor interface

along with identifying previously undetermined surface reconstructions. The

electronic properties of the system were examined by taking STS spectra, which reveal

how the adsorbate changes the electronic properties of the semiconductor after

bonding. In addition, DFT was used to confirm experimental results along with

predicting other adsorbate/semiconductor interactions.

CHAPTER ONE

Direct and Indirect Causes of Fermi Level Pinning at the SiO/GaAs Interface

1.1 Abstract

The correlation between atomic bonding sites and the electronic structure of SiO on GaAs(001)-c(2×8)/(2×4) was investigated using scanning tunneling microscopy (STM), scanning tunneling spectroscopy (STS), and density functional theory (DFT). At low coverage, STM images reveal that SiO molecules bond Si end down; this is consistent with Si being under coordinated and O being fully coordinated in molecular SiO. At ~5% ML (monolayer) ML coverage, multiple bonding geometries were observed. To confirm the site assignments from STM images, DFT calculations were used to estimate the total adsorption energies of the different bonding geometries as a function of SiO coverage. STS measurements indicated that SiO pins the Fermi level midgap at ~5% ML coverage. DFT calculations reveal that the direct causes of Fermi level pinning at the SiO GaAs(001)-(2×4) interface are a result of either local charge buildups or the generation of partially filled dangling bonds on Si atoms.

1.2 Introduction

Early attempts to fabricate a GaAs-based metal-oxide semiconductor filed-effect transistor device focused on using either SiO_2[7,16-19] or the native oxide of GaAs[3,8,20] as the gate dielectric. Unfortunately, both oxides were found to induce states within the band gap, pinning the Fermi level.[21-23] The Fermi level is considered pinned when an external potential can no longer modulate the Fermi level position making a device inoperable. In the case of GaAs's native oxide, Fermi level pinning was initially attributed to excess As on the surface,[24-28] but an atomic level understanding of the oxide/GaAs interface did not exist. Since the two conventional oxides (SiO_2 and the native oxide) pin the Fermi level, a broad search of other oxides was needed to find a gate dielectric material that would passivate the GaAs surface, leaving the Fermi level unpinned.

In an effort to find an appropriate oxide, research efforts have recently shifted to include not only macroscopic studies [capacitance voltage (CV), photoluminescence, etc.] but also microscopic studies [scanning tunneling microscopy (STM) and scanning tunneling spectroscopy (STS)]. These microscopic studies (Hale *et al.*[29,30] and Negoro *et al.*[31]) have given insight into the atomic structures of adsorbates bound to the GaAs(001)-c(2×8)/(2×4) surface and revealed that the cause of the Fermi level pinning was not excess As on the surface.

Several macroscopic studies have been performed on the SiO/GaAs interface,[32-35] but none on the atomic level. Building on previous work, the results presented in this manuscript show how the exact atomic placement of SiO adsorbates influences the electronic structure of SiO/GaAs(001)-c(2×8)/(2×4) system.

1.3 Experimental Techniques

Experiments were performed in an UHV chamber with a base pressure of $3×10^{-10}$ Torr. The chamber is equipped with low energy electron diffraction (LEED) and a Park Scientific AutoProbe VP STM with STS capabilities. As$_2$-capped (~25 nm) n- and p-type molecular beam epitaxially grown GaAs samples were used for the study, with Si and Be dopant concentrations of $2×10^{17}$ cm^{-3}, respectively. Both n- and p-type samples appear identical in STM images but differ in electronic properties.

To prepare the samples for STM, a thermal decapping procedure was employed. Initially, the samples were degassed at 200ºC for at least 2 h to remove the weakly bound adsorbates such as water. This was followed by 10-50 cycles of 2 min temperature ramps to 420ºC followed by instantaneous drops in temperature and stabilization at 50ºC for another 2 min, to remove the As$_2$ cap. These cycles were repeated until there was no pressure rise due to As desorbing from the surface. A plot of the temperature ramps and subsequent pressure rises can be found on EPAPS.[36] Following the decapping procedure, the surface order was verified by both LEED and

STM.   Variable tip-sample separation STS (dI/dV) measurements were taken utilizing an ac modulated input signal and a lock-in amplifier.[37-39]   STS was used to confirm that the clean surface was unpinned.

Once the atomic and electronic structures of the clean GaAs(001)-c(2×8)/(2×4) surface were characterized, the samples were dosed with molecular SiO. The SiO was deposited from sintered SiO powder heated to 950ºC in a differentially pumped effusion cell. SiO powder has been shown to evaporate congruently as molecular SiO with no other oxide species, at low evaporation temperature and pressure,[27-29] similar to our operating conditions.   The deposition was performed at a main chamber pressure of ~2x10^{-8} Torr with the sample held at ~14ºC; postdeposition anneals were found to have no influence on the bonding geometries. After SiO deposition, STM and STS measurements were again used to characterize the surface.

1.4 Experimental Results and Discussion

A.   Scanning tunneling microscopy images and line scans

Figure 1(a) is a filled-state STM image of the clean GaAs(001)-c(2×8)/(2×4) surface. The bright rows that run in the $[\bar{1}10]$ direction are comprised of first-layer electronegative As dimer pairs.[40-46] A ball-and-stick diagram of the GaAs(001)-(2×4) surface is provided in Fig. 1(b). The As dimers that reside in the troughs are not

resolved with these imaging conditions due to tunneling between the trough edge atoms and the tip, prohibiting the tip from fully entering the trough.[47]

The actual GaAs(001) surface structure is a mixture of the $c(2\times8)$ and (2×4) surface reconstructions.[41,47] The difference between the two reconstructions is subtle: in the $c(2x8)$ surface structure, consecutive As dimer rows are staggered by ½ of a unit cell along the $[\bar{1}10]$ direction, instead of lining up across the trough, as seen in the (2×4) reconstruction. However, both structures have the same electronic properties and few defects ($< 2\%$). The two most common imperfections (missing As dimers and excess As) observed via STM are a result of the thermal decapping procedure. Missing As dimers result from the surface getting slightly too warm and are depicted in the ball-and-stick diagram in Fig. 1(b). Excess As is the most common imperfection and occurs from the nonuniform heating of the sample and is imaged as bright patches on the dimer rows.

Once the clean surface has been confirmed using LEED and STM, SiO is deposited. Figure 2(a) shows a large-scale image of the GaAs surface after depositing SiO for 1 min on room-temperature GaAs(001)-$c(2\times8)/(2\times4)$, resulting in ~5% ML coverage. The bright patches on the rows and troughs are the SiO bonding sites, some of which have been encircled in black. SiO is not confused with excess As because the latter generally forms clumps which span several rows. A magnified STM image showing three different SiO bonding sites is presented in Fig. 2(b); line scan analysis was performed on the STM image to help deduce the bonding sites. Figure 2(c) (top)

is a line scan of the adsorption site (bright patch) in the upper left hand corner of Fig. 2(b): this site images 4 Å long and 1.5 Å tall. It is proposed that this site consists of one SiO molecule inserting into an As dimer, denoted as a "single site." A side-on model of the proposed row single site is shown under the line scan in Fig. 2(c) (top) and a top-down view is seen in Fig. 2(f) (site 1). The other experimentally observed row site is seen in the bottom center of Fig. 2(b). Line scan analysis [Fig. 2(c) (bottom)] reveals that this site measures twice as long in the $[\bar{1}10]$ direction as the single site and is of the same height. This site is proposed to be a "compact double site," which consists of a SiO molecule inserting into an As dimer and an additional SiO molecule inserting between the insertion dimer and an adjacent dimer. A side-on model of the row compact double site is seen under the line scan in Fig. 2(c) (bottom) and a top-down model of the site is shown in Fig 2(f) (site 2).

Both of the sites observed on the row are also proposed to occur in the trough region, in addition to two unique trough sites. Three of the trough sites (single, compact double, and triple sites) are not casually observed in the STM images. This is due to the lack of trough resolution at these tunneling conditions, as discussed previously. These sites, however, can be characterized by line scan analysis. Line scan analysis shows that the trough single [Fig. 2(d) (top)] and the trough compact double [Fig. 2(d) (middle)] are the same length in the $[\bar{1}10]$ direction as the corresponding sites on the row. Side-on models of the single and compact double sites are seen under their line scans. The third type of trough site, also observed only by

line scan analysis, has no row-type analogue and measures 12 Å long in the $[\bar{1}10]$ direction [Fig. 2(d) (bottom)]. This site is proposed to be two SiO molecules inserting into adjacent dimers and a third SiO molecule inserting between them; this site is denoted as a "triple site."

Another site that is only observed in the trough is shown via a side-on model in Fig. 2(e). Unlike the trough sites in Fig. 2(d), the site in Fig. 2(e) is consistently observed in experimental STM images. This site measures ~1 Å higher than the row, which is too tall to be a simple insertion site (i.e., it must contain stacked SiO molecules). Although such a conclusion cannot be reached exclusively from STM images, this site is proposed to be a "pyramid site." Other data will be presented that will further substantiate this site assignment. Side-on models along the [110] and $[\bar{1}10]$ directions, along with line scans of the pyramid site, are seen in Fig. 2(e). In addition, a top-down model of the pyramid site is shown in Fig. 2(f) (site 4).

The STM images strongly suggest that SiO bonds Si end down, which is consistent with simple chemical principles. The valence shell of a Si atom contains four electrons and is sp^3 hybridized, therefore, it typically forms four bonds. An O atom contains six valence electrons and typically forms only two bonds, leaving two filled dangling bonds (i.e., two lone pair orbitals). Assuming that SiO inserts Si end down, Si can form one bond with each of the surface As atoms in the dimer and form a double bond with the O atom. This allows both the O atom and the Si atom to satisfy the requirements of the octet rule.

The 1.5 Å height difference observed by STM between the SiO molecule and the dimer row (seen in the row single and compact double sites) is also consistent with SiO inserting Si end down. The images obtained from STM are a convolution of atomic position, local density of states, and electron density. If SiO inserts Si end down, the majority of the most weakly bound electron density (i.e., closest to the Fermi level) should be concentrated in the double bond between the Si and O since the highest occupied molecular orbital is concentrated in that area. For SiO bonded Si end down, the double bond should be approximately 1.5 Å above the As dimer row, which is in agreement with the experimental observations. Furthermore, the electron density in the filled dangling bonds of the O atoms have an energy level far below the Fermi level, prohibiting electrons from tunneling out of those orbitals and into the tip.[30,48,49] If SiO were to insert O end down, the majority of the electron density near the Fermi level would be concentrated in the nonbonding orbitals of Si. This would result in a taller site than is experimentally observed.

The trough sites (single, compact double, triple, and pyramid sites) are expected to image at two different heights. In structural models, the trough is ~3 Å deep. However, experimentally the average trough depth is ~1.5 Å, therefore, anything below this height will not be directly observed. Since the trough single, compact double, and triple sites are only expected to image at ~1.5 Å from the bottom of the trough, one would not expect these sites to have prominent features in STM images, which is consistent with the STM data shown in Fig. 2(d). In contrast, the top double bond in the trough pyramid site is located ~3 Å from the bottom of the trough;

therefore, one might expect the trough pyramid site to image level with the row (since the trough is ~3 Å deep). Experimentally the trough pyramid site is found to image ~1 Å above the row, slightly higher than one might predict. The height difference between the predicted and actual image height is attributed to the top O atom having a greater density of states at an energy closer to the Fermi level than a typical surface O atom (as will be discussed later in the paper). Therefore, unlike most surface O atoms, the top O atom in the trough pyramid site is imaged, resulting in the trough pyramid site imaging ~1 Å above the row.

B.   Scanning tunneling spectroscopy

In addition to the STM images of the various SiO adsorption sites, STS (surface electronic structure) measurements were also taken using the variable tip-sample separation method developed by Feenstra and co-workers.[37-39] With this technique, GaAs(001) was found to have a band gap of 1.4 V. Figure 3(a) presents $(dI/dV)/(\overline{I/V})$ vs V spectra [which are proportional to the density of states (DOS)] for clean n- and p-type GaAs(001)-c(2×8)/(2×4) surfaces respectively. The Fermi level for all given $(dI/dV)/(\overline{I/V})$ curves resides at 0 V. From the data, it can be seen that the Fermi level for n-type GaAs(001)-c(2×8)/(2×4) resides near the conduction band and the Fermi level for p-type GaAs(001)-c(2×8)/(2×4) resides near the valence band, as expected. These results are typical of unpinned n- and p-type surfaces. Figure 3(b) shows STS spectra that were taken after depositing ~5% ML SiO on n-

and *p*-type GaAs(001)-*c*(2×8)/(2×4), respectively. In both cases, the bands are shifted, relocating the Fermi level to midgap; this is consistent with a pinned surface, indicating that Fermi level pinning occurs at SiO coverages as small as ~5% ML.

From the ball-and-stick diagram in Fig. 2(f), it can be seen that none of the proposed sites liberate As when SiO is deposited onto the surface. Furthermore, from the STM image in Fig. 2(a), no excess As deposits are seen. Therefore, excess As is certainly not the cause of the Fermi level pinning in this case.

C.   Local charge buildup model

To deduce the cause of the Fermi level pinning, a closer look is taken at the transfer of electrons during SiO bonding to the surface using simple molecular orbital models. The bonding electrons of the system are located in the tetrahedral (sp^3 hybridized) orbitals of the As and Si atoms. Prior to bonding with the surface, the Si atom in a SiO molecule has two half-filled dangling bonds. In order to calculate a minimum number of electrons in the dangling bonds of the surface As atoms, the rules of the standard electron counting model are applied. These rules state that atoms contribute the same number of electrons to surface bonds as they do in the bulk material (i.e. As gives 5/4 of an electron to Ga in the bulk, therefore it gives 5/4 of an electron to a bond with a surface Ga atom) and atoms bonded to like atoms each give one electron to the bond.[50] Therefore, since the dimer As atoms are each bonded to

two Ga atoms and one As atom, the dangling bond on dimer As atoms are left with at least 3/2 electrons.

Figure 4(a) is a ball-and-stick diagram depicting the formation of a single site, with arrows denoting the movement of electrons. In the formation of the single site, the SiO molecule inserts into the As-As bond and forms two new Si-As bonds with the surface. Each time an As-As bond is broken, each As atom gains one electron. In order to form a Si-As bond, the bond receives one electron from the dangling bond in Si and one electron from the As atom. The number of electrons needed to form the bond is exactly equal to the number of electrons available between the Si and As atoms (i.e., two electrons); therefore, no buildup of extra electrons, or local charge, on any of the atoms associated with this adsorption site is expected.

Unlike the single site, the compact double site is expected to have a small local charge buildup. The formation of the compact double site is shown in Fig. 4(b). When a compact double site forms, one SiO molecule inserts into an As dimer and the other SiO molecule inserts between that same dimer and the neighboring As dimer. The distal As atom in the neighboring dimer (that is not involved in the SiO bonding) may redimerize if the energy barrier is low enough. In the formation of the compact double site, four Si-As bonds are created. The center As atom is forced to form a total of four bonds (two Ga-As and two Si-As); therefore, the As atom can no longer have any dangling bonds. Since the preexisting dangling bond had 3/2 electrons, an excess of ½ of an electron remains after the formation of the Si-As bonds. This excess ½ of

an electron may then be incorporated into the local bond network and/or the partially filled dangling bonds on the outer As atoms, potentially giving the dangling bonds a minimum charge of 7/4 electrons, as seen in Fig. 4(b).

The triple and pyramid sites are expected to have larger local charge buildup, as depicted in Figs. 4(c) and 4(d), respectively. In the case of the triple site, three SiO molecules form six Si-As bonds with the surface [Fig. 4(c)]. Since the center two As atoms can no longer have dangling bonds, there remains an excess charge of one electron that must be incorporated into the local system, which can result in the outer As atoms' dangling bonds possessing a minimum of two electrons each. This local charge buildup should be large enough to perturb the local electronic structure and potentially pin the Fermi level.

The pyramid site is the most complicated SiO adsorption site. From Fig. 4(c), it can be seen that there are two major sources of charge buildup. The first source is the center As atom that forms two Si-As and two Ga-As bonds, similar to the compact double site. This generates an excess of ½ electron that needs to be incorporated into the local system (i.e. bond network and/or outer As atoms' dangling bonds). The second source of charge buildup occurs as a result of the undercoordination of the bottom Si atoms. In the SiO pyramid, the bottom O atoms are single bonded to two different Si atoms (as opposed to being double bonded to a single Si atom as in all of the other adsorption geometries). Therefore, the bottom Si atoms are sp^3 hybridized while all of the other Si atoms are sp^2 hybridized. Since the bottom Si atoms form

three fully formed bonds (one Si-O and two Si-As) they have an additional half-filled dangling bond. These half-filled dangling bonds are predicted to generate a state in the band gap region, thereby pinning the surface.

This simple model implies that there may be two distinct direct causes of Fermi level pinning in the SiO/GaAs(001)-c(2×8)/(2×4) system: the buildup of local charge (triple site) and partially filled dangling bonds on Si atoms (pyramid site). The validity of the local charge buildup model is further examined with DOS, projected density of states (PDOS), and atomic charge analysis from density functional theory (DFT) calculations.

1.5 Computational Results and Discussion

A.   Enthalpies of adsorption

Plane-wave (periodic boundary) DFT calculations were performed with the Vienna *ab initio* simulation package (VASP) code.[51-54] The surface of interest was modeled using an eight layer GaAs(001) H-terminated slab with the (2×4) surface reconstruction. The bottom four layers of the slab were frozen to help simulate bulk properties. The calculations were performed using the Perdew-Burke-Ernzerhof[55] (PBE) variant of the general gradient approximation. Projector augmented wave (PAW) potentials were used to represent the atoms (as supplied with VASP).[56,57] The plane wave cutoff energy was set to 400 eV, and the *k*-point sampling utilized was a 4×4×1 Monkhorst-Pack[58] *k*-point sampling scheme resulting in a total of four irreducible *k*-points in the first Brillouin zone. The structures were considered adequately relaxed once the interatomic forces were below 0.01 eV/Å.

The errors associated with these calculations are not straightforward to estimate. There are two types of errors that arise in DFT calculations: convergence errors and method errors. Convergence errors include both errors related to the choice of convergence parameters (plan-wave cutoff, *k*-points, slab thickness, vacuum thickness, etc.) as well as relaxation parameters (maximum allowed forces on atoms). If the appropriate computational parameters are chosen, the convergence errors should

be negligible compared to the method errors. The method errors encompass the errors inherent to the chosen computational method (exchange correlation functional, various approximations, atomic potential, etc.) and can be further broken down into two subcategories: absolute method errors and relative method errors (or uncertainties).

Absolute method error refers to how well the computational results match with experimental data. Paier *et al.* calculated the mean absolute error (absolute method error), with respect to experimental values, of the G2-1 test set as 0.37 eV using VASP, with PAW potentials and the PBE exchange correlation functional[59] (the same as was used in the work presented here). Although the absolute method error was calculated for a large set of widely varying molecular systems (55 in total), the test set does not include any adsorbates on surface, which would be closer to the systems in the current study. Additional literature searches revealed no systematic studies of absolute method errors for adsorbates on surfaces. Although the absolute method error in this study is potentially as large as 0.37 eV, the relative method errors are expected to be much smaller.

The relative method error refers to the uncertainty in the total energy difference between two similar adsorption sites. When comparing the relative total energies of a single adsorbate at two different sites on a surface, the relative error is the most important error. For example, if the relative method uncertainty is ± 0.10 eV and two structures, both having one adsorbate bonded in different locations, have adsorption energies of 1.00 and 1.05 eV then the two structures are considered to be

degenerate due to computational uncertainties. A search of the literature revealed no systematic study of the relative method error for adsorbates on surfaces. However, experts in the field report differences in binding energy at similar absorption sites on the same surface of ± 0.10 eV to be significant using computational techniques similar to the ones in the present manuscript.[60,61] Therefore, we will assume a relative method error of ± 0.10 eV in the current study. Since the differences in calculated absorption energy are usually much larger than ± 0.10 eV, the overall qualitative trends in both the calculations and the experiments should be in good agreement.

Both experimentally observed and nonobserved (but chemically possible) sites were modeled in an effort to verify the bonding geometries that were deduced from STM images. Tables I and II show top-down views of the calculated row and trough bonding sites, respectively, and include their corresponding enthalpies of adsorption, enthalpies of adsorption per SiO, and corrected enthalpies of adsorption per SiO (in structures that have an undimerized As atom). In order to calculate the row As dimerization energy, two clean slabs with eight row As atoms were modeled: one with the row As atoms dimerized, and the other with row As atoms undimerized. The energy difference between these two slabs amounts to four times the As dimerization energy. A similar calculation was preformed to calculate the trough dimerization energy.

The DFT total energy calculations show that many of the row and trough sites are nearly energetically degenerate (Tables I and II). All of the sites that are nearly

degenerate come from having two single sites in immediate proximity of each other (i.e., two SiO atoms in adjacent dimers in the [110] or [$\bar{1}$10] direction which are referred to as the "horizontal double" and "vertical double," respectively). Therefore, it is only necessary to present calculations for the row and trough single sites throughout the rest of the paper.

The row/trough compact double sites were found to be less stable than the row/trough single sites by ~0.24 eV per SiO. In the row, the compact double site has a total corrected ΔH_{ads} of -1.74 eV (double the corrected value of -0.87 eV/SiO from Table I). The compact double site is a combination of a single site and an insertion site between As dimers. Since the row compact double site receives -1.08 eV of stability from the single site, it is deduced that the insertion site between As dimers only provides a -0.66 eV gain in stability. However, in the trough, the compact double site has a total corrected enthalpy of reaction of -2.12 eV; therefore, it receives an additional -0.80 eV of stabilization from the addition of the second SiO molecule between the dimers. Since the compact double site is the building block for sites that contain three SiO molecules (triple and pyramid sites), this data would imply that complexes containing three SiO molecules should be more stable in the troughs than in the rows.

Experimentally, the biggest difference in row and trough sites occurs in sites that have three SiO molecules in them (triple and pyramid sites). On the row, there are no experimentally observed sites that contain three SiO molecules, while in the

trough two different sites with three SiO molecules are experimentally observed. Calculations were attempted on both the row triple and row pyramid sites. The row triple site was found to be significantly less stable than the experimentally observed row sites (single and compact double sites), and the row pyramid site was altogether computationally unstable (i.e., the pyramid consistently fell apart during geometric optimization). In contrast, the trough triple and pyramid sites were found to be stable by DFT calculations. This stabilization is attributed to the Ga atoms that protrude into the trough. An analysis of simple Coulombic potentials indicates that if the Ga atoms that protrude into the trough have as few as ~$0.08e^-$ in their dangling bonds, then the SiO molecules in the trough receive ~0.1 eV of stabilization per SiO molecule.

To determine if it is reasonable to assume that trough edge Ga atoms have a charge of $0.08e^-$, an atomic charge analysis was performed. For this analysis, the Bader method for the calculation of atomic charges was employed. In this method, the charge density minima around each atom defines where the division of charge between atoms occurs. The charge density encapsulated by these minima are then integrated to yield approximate atomic charges.[62] In order to determine the approximate number of electrons in a dangling bond on an edge Ga atom "relative" atomic charges (the difference in atomic charge between an edge Ga atom and a Ga atom in the bulk) are calculated. The relative charge was found to be ~$0.09e^-$. Since the number of electrons in the dangling bonds of the Ga atoms that protrude into the

trough is greater than the charge needed to stabilize the trough sites by 0.1 eV per SiO, the trough sites should be expected to be more stable than the row sites.

B.   Total energy versus chemical potential

The DFT adsorption energy calculations indicate that the lowest energy structures (per unit SiO) on the row and in the trough are the single sites (see Table I and II). However, the single sites are not the most prevalent sites observed in STM images. In order to reconcile this discrepancy between theory and experiment, the SiO coverage needs to be taken into account. As the SiO coverage increases, the SiO chemical potential increases, altering the most energetically preferred adsorption geometries. A total SiO chemical potential plot was constructed using the method described by Qian and *et al.*[63] and normalized to the appropriate energy range.[43,46,64] Figure 5(a) displays the lowest energy row and trough sites on one graph, clearly illustrating the fact that the trough sites are slightly more energetically preferred than the row sites. At first glance, the STM images may suggest that trough sites are not preferred over row sites; however, three of the trough sites (single, compact double, and triple sites) are not readily observed due to the previously discussed trough imaging issue, and therefore, the number of trough sites is always underestimated. Taking this into account, the experimental images are believed to verify that SiO preferentially bonds in the trough and, therefore, agree with the theoretical results in Fig. 5(a).

To study the effects of varying SiO coverage on the stability of row sites, a chemical potential plot including only row sites [Fig. 5(b)] was employed. As SiO coverage increases, the lowest energy site changes from the row single site to the row vertical double site. The row triple site maintains a significantly higher energy than the other structures and would not become the lowest energy structure until the chemical potential of SiO reaches ~0.8 eV. This explains why the row triple site is not observed experimentally.

The effect of SiO coverage in the trough was also explored by constructing a total energy versus chemical potential plot for the trough sites [see Fig 5(c)]. This plot reveals that the lowest energy site in the trough changes from the trough single to the trough vertical double and finally to the trough pyramid site, as the SiO coverage increases.

C.   Bond angles and lengths

To verify the local charge buildup model presented in Sec. III C, the SiO bonding angles and lengths were examined for the lowest energy structures in the DFT calculations (Fig. 6). The local charge buildup model (Fig. 4) predicted that all of the Si atoms would be sp^2 hybridized except for the two Si atoms in the pyramid site that have partially filled dangling bonds, which were predicted to be sp^3 hybridized. The relaxed DFT calculated structures (Fig. 6) reveal that the Si-O bond lengths are all ~1.55 Å, except for the Si atoms in the pyramid site that have partially filled dangling

bonds, which have Si-O bond lengths of 1.64 Å. This is consistent with what was predicted because double bonds are shorter than single bonds. In ideal sp^2 and sp^3 bonding structures, the bond angles should be 120º and 109.5º, respectively. In the structures that only contain sp^2 Si atoms [row single, row compact double, trough single, trough compact double, and trough triple Fig. 6(a)-(e)], the bond angles (As-Si-As and As-Si-O) calculated using DFT only deviate a maximum of 15º from their ideal values. Conversely, in the trough pyramid site, all of the angles greatly deviate from the ideal angles. This suggests that the simple model of having one electron in the dangling bonds on the bottom Si atoms in the pyramid site is oversimplified and some of the charge has redistributed throughout the bonding network as well as into the dangling bond of the Si atom.

D.   Scanning tunneling microscopy simulations

Tersoff-Hamann-style STM simulations[65] of the experimentally observed SiO adsorption sites were performed to further substantiate the assigned bonding geometries. The STM simulations are found in Fig. 7, including top-down views of the structures overlaid on the simulated images. The STM simulations of the row single [Fig. 7(a)], row compact double [Fig. 7(b)], and trough pyramid [Fig. 7(f)] sites are in good agreement with experiments. However, the simulated trough single [Fig. 7(c)], trough compact double [Fig. 7(d)], and trough triple [Fig. 7(e)] sites appear much higher/brighter than experimentally observed sites because these simulations do

not account for the physical geometry of the tip. In experiments, the STM tip's inability to fully enter the trough causes the trough to image much more shallow than found in theoretical structural models (~1.5 Å versus ~3.0 Å deep). Therefore, any trough site (single, compact double, or triple site) that is calculated to image at 1.5 Å or below will not be directly observed in STM images but will be readily seen in STM simulations. The STM simulations, along with the total energy versus chemical potential data, confirm that the site assignments from experimental STM images are indeed correct.

E.   Density of states and projected density of states

DOS and PDOS calculations were performed on the experimentally observed sites in an effort to elucidate the cause of the Fermi level pinning. These theoretical electronic structures differ slightly from the experimental (dI/dV) curves because the computational slabs are much too small for the inclusion of dopants and, therefore, are essentially intrinsic GaAs. In addition, the position of the Fermi level between the valence and conduction bands is arbitrary, so for ease of comparison all the DOS and PDOS curves have been aligned at the valence bands. As a result, a modeled surface is considered unpinned if there are no states found to exist between the valence and conduction band edges.

The compact double sites and the trough pyramid site have surface As atoms that are not dimerized in the computational model (experimentally, these atoms may either remain undimerized or, if the energy barrier is low enough, they may redimerize down the row). These undimerized As atoms induce large states within the band gap region. Although the undimerized As atoms might play an indirect role in the Fermi level pinning, it is important to also explore whether the adsorbed SiO molecules themselves play a direct role in the Fermi level pinning. To negate the effects of the undimerized As atoms, H atoms were used to passivate the dangling bonds on the undimerized surface As atoms to simulate As redimerization. Once the H atoms were utilized, the states caused by the undimerized As atoms disappeared, leaving only the states directly induced by the SiO molecules. Both H atoms with a charge of 1 electron and 0.75 electrons were found to passivate the surface. The results from the calculations using one electron H atoms are presented because the electron counting model states that As atoms donate only one electron to bonds with other As atoms.[50]

The total DOS for the row and trough single sites are given in Fig. 8. The DOS shows that no states reside in the band gap. Therefore, the single sites are expected to leave the Fermi level unpinned.

A summary of the electronic structures for the row and trough compact double sites is given in Fig. 9(a) along with a top-down view of the structures used in the calculations, Fig 9(b) (note: with H passivation). The DOS [Fig. 9(a)] reveals that for the compact double sites, there are no states between the valence band and conduction

band edges. However, the row compact double site has a slightly narrower band gap due to conduction band edge states. Since there are no states in the band gap region the compact double sights is considered to leave the Fermi level unpinned.

A summary of the electronic structures for the trough triple site is presented in Fig. 10. The DOS for the trough triple site shows that a state resides near the conduction band edge [Fig. 10(a)]. PDOS [Fig. 10(c) and 10(d)] calculations reveal that the state generated from the trough triple site resides on the surface As, Si, and O atoms. It is likely that the SiO trough triple site contributes to the experimentally observed Fermi level pinning.

Similar to the compact double site, the formation of the trough pyramid site might also result in the generation of undimerized As atoms. The electronic structure for the H-passivated trough pyramid site is presented in Fig. 11. The DOS [Fig. 11(a)] for the trough pyramid site shows that a double state resides almost in the middle of the band gap. It is possible that the two states might represent an acceptor and a donor state. The PDOS reveals [Fig. 11(c) and 11(d)] that this state extends across multiple atoms. These atoms include the SiO molecules and the As atoms in the trough; however, these states do not extend into the bulk material and are purely surface states.

F.   Atomic charge analysis

An atomic charge analysis can be used to quantify the local charge buildup in these adsorption structures and explain the appearance of band gap states in the trough triple and pyramid sites. Atomic charges can be calculated using the Bader method discussed previously.[62] The relative charges are calculated from differences in atomic charges between the clean surface and a surface containing the SiO molecules (Fig. 6). In order to calculate relative charges for the Si and O atoms, the single sites were used as the standard. For row sites the row single was used as the zero point, and for trough sites the trough single was used as the zero point. The total (a sum of the surface As, Si, and O atoms) charge buildup is presented under each of the structures in Fig. 6.

Fig. 6 clearly shows that larger charge buildups occur on the interior As atoms than on exterior ones. This is consistent with what was predicted by the local charge buildup model. A subtlety that was not predicted by the local charge buildup model is that even when no interior As atom is present [as in the case with the single sites, Fig. 6(a) and (c)], SiO still donates small amounts of charge to the surface As atoms; this result is understandable considering the difference in electronegativity between As and Si (2.18 vs 1.90, respectively).[66] Another assumption that the local charge buildup model made was that excess charge would preferentially migrate to the dangling bonds on the exterior As atoms. However, the atomic charge analysis revealed that the dangling bonds could only accommodate some of the extra charge, leaving large charge buildups on the interior As atoms and other Si and O atoms. Therefore, a more

reliable way of quantifying the local charge buildup is by looking at the total charge buildup on all of the surface atoms (As, Si, and O).

Atomic charge analysis can be used to explain why the DOS indicated that the SiO pinned the Fermi level for some of the bonding geometries and left the Fermi level unpinned for other geometries. The DOS suggested that the Fermi level was unpinned for the row and trough single and compact double sites. Figures 6(a) and 6(c) shows that the single sites have a total charge buildup of ~0.41e^-. While the compact double sites, Figs. 6 (b) and (c), have a total charge buildup of ~0.66e^-. The local charge buildup model predicted that there would be an increase in charge every time an additional As atom was added to the SiO bonding system. Following this logic the trough triple site would be expected to have an even larger charge buildup than the compact double sites; the Bader atomic charge analysis verifies this prediction (0.80e^-). Although the difference in charge buildups between the compact double and triple sites is seemingly small, it leads to a rather large charge buildup in a small region, which probably induces the band edge states seen in the DOS [Fig. 10 (c) and 10(d)].

Although the trough pyramid site [Fig. 6(f)] is predicted to have a comparable charge buildup to the trough compact double site, it has an additional problem: the formation of partially filled dangling bonds on the bottom two Si atoms. This can be seen by the large relative charge of 0.34e^- (per Si) which resides on the bottom Si atoms in the trough pyramid site. This is consistent with Si atom having a partially

filled dangling bond. As previously discussed, the Si-O bond length also indicates the presence of a single bond which would be consistent with a partially filled dangling bond on the lower Si atoms of the trough pyramid site. These partially filled dangling bonds almost certainly create the midgap states in the DOS [Fig. 11(a)].

1.6 Conclusion

Microscopic experimental techniques (STM and STS) and DFT calculations show that the exact bonding geometries of SiO on GaAs(001)-$c(2\times8)/(2\times4)$ determines the electronic structure. While some of the SiO chemisorption sites leave the Fermi level unpinned, other SiO chemisorption sites pin the Fermi level. The Fermi level pinning in the trough triple and pyramid sites was attributed to two direct causes: the buildup of charge on several consecutive As atoms and/or the formation of partially filled dangling bonds on some of the Si atoms. In addition, some of the bonding sites (row compact double, trough compact double, and trough pyramid sites) might cause indirect pinning by generating undimerized As atoms which were shown to pin the Fermi level. The Fermi level pinning seen when SiO chemisorbs to the GaAs(001) surface is not due to the intrinsic properties of GaAs(001) and SiO but due to the specific bonding geometries at the interface.
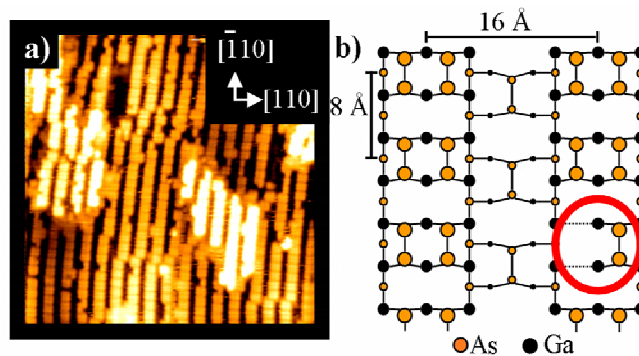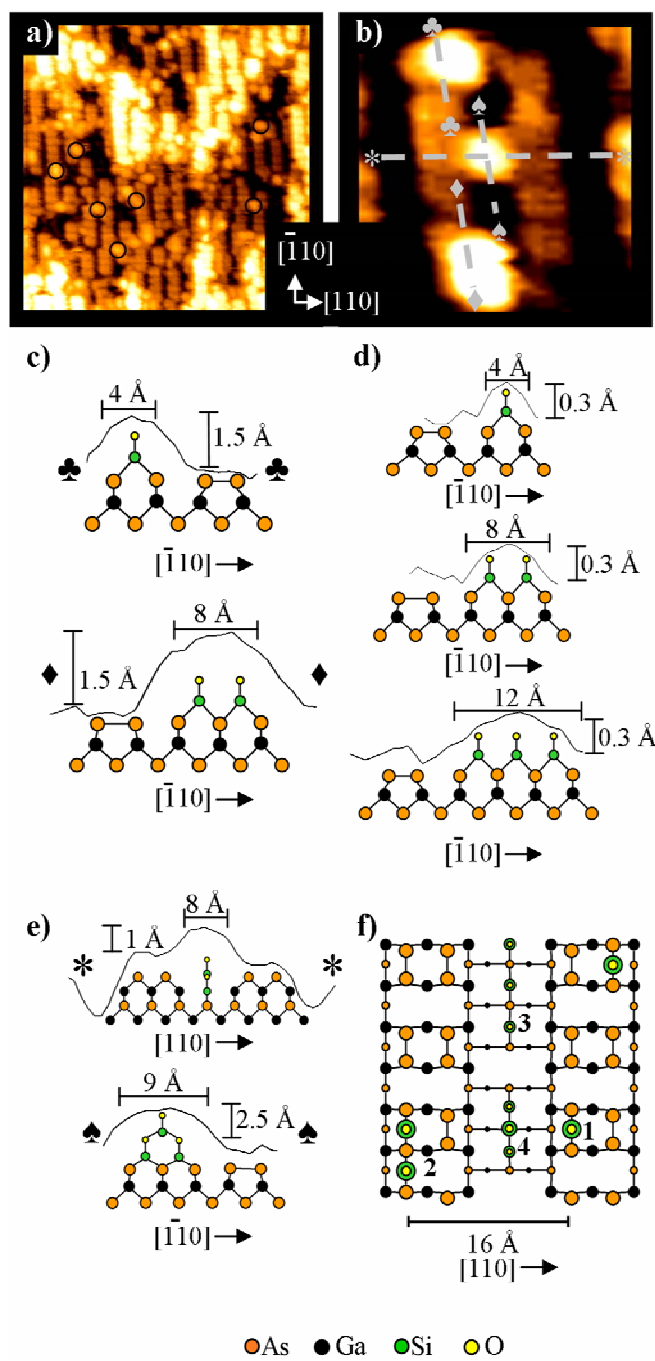
1.7 Figures

FIGURE 1.1 (a) 300 × 300 Å^2 filled-state STM image (V_s=-3 V, I_t=0.2 nA) of a clean GaAs(001)-c(2×8)/(2×4) surface. (b) Ball-and-stick diagram showing the atomic positions of the GaAs(001)-c(2×8)/(2×4) surface reconstruction with one of the most common defects, a missing As dimer, circled in red.

FIGURE 1.2 (a) 300 × 300 Å^2 filled-state STM image (V$_s$=-3 V, I$_t$=0.2 nA) of the GaAs(001)-c(2×8)/(2×4) surface with ~5% ML coverage of SiO. Some of the SiO bonding sites have been circled in black. (b) 50 × 50 Å^2 filled-state STM image (V$_s$=-3 V, I$_t$=0.2 nA) of row single, row compact double, and trough pyramid sites. (c) Line scans and ball-and-stick diagrams of the two row sites: the single (top), and compact double (bottom) sites. (d) Line scans and ball-and-stick diagrams of the trough sites that are differentiated using line scan analysis: the single (top), compact double (middle), and triple (bottom) sites. (e) Line scans and ball-and-stick diagrams of the trough pyramid site perpendicular, [110] (top), and parallel,[$\bar{1}$10] (bottom), to the trough. (f) Top-down ball-and-stick diagram of some of the most commonly observed SiO adsorptions sites; the sites are labeled as indicated, "1"a row single site, "2" a row compact double site, "3" a trough triple site, and "4" a trough pyramid site.

a) b)

[$\bar{1}$10]
[110]

c) d) e) f)

4 Å
1.5 Å
♣ ♣
[$\bar{1}$10] →

8 Å
♦ 1.5 Å ♦
[$\bar{1}$10] →

4 Å
0.3 Å
[$\bar{1}$10] →

8 Å
0.3 Å
[$\bar{1}$10] →

12 Å
0.3 Å
[$\bar{1}$10] →

1 Å
8 Å
* *
[110] →

9 Å
2.5 Å
♠ ♠
[$\bar{1}$10] →

3
2 4 1
16 Å
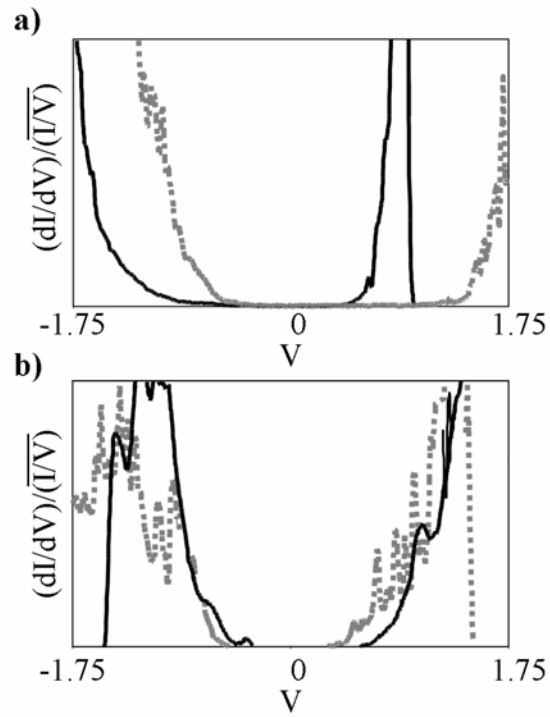[110] →

● As ● Ga ● Si ○ O

FIGURE 1.3 STS measurements of (a) clean *n*-type (thick solid line) and *p*-type (gray dashed line) GaAs(001)-*c*(2×8)/(2×4), and (b) ~5% ML coverage of SiO on *n*-type (thick solid line) and *p*-type (gray dashed line) GaAs(001)-*c*(2×8)/(2×4).   Note that both clean *n*- and *p*-type GaAs(001)-*c*(2×8)/(2×4) STS plots (a) exhibit electrically unpinned surfaces, while the SiO deposited surfaces (b) are found to be pinned.
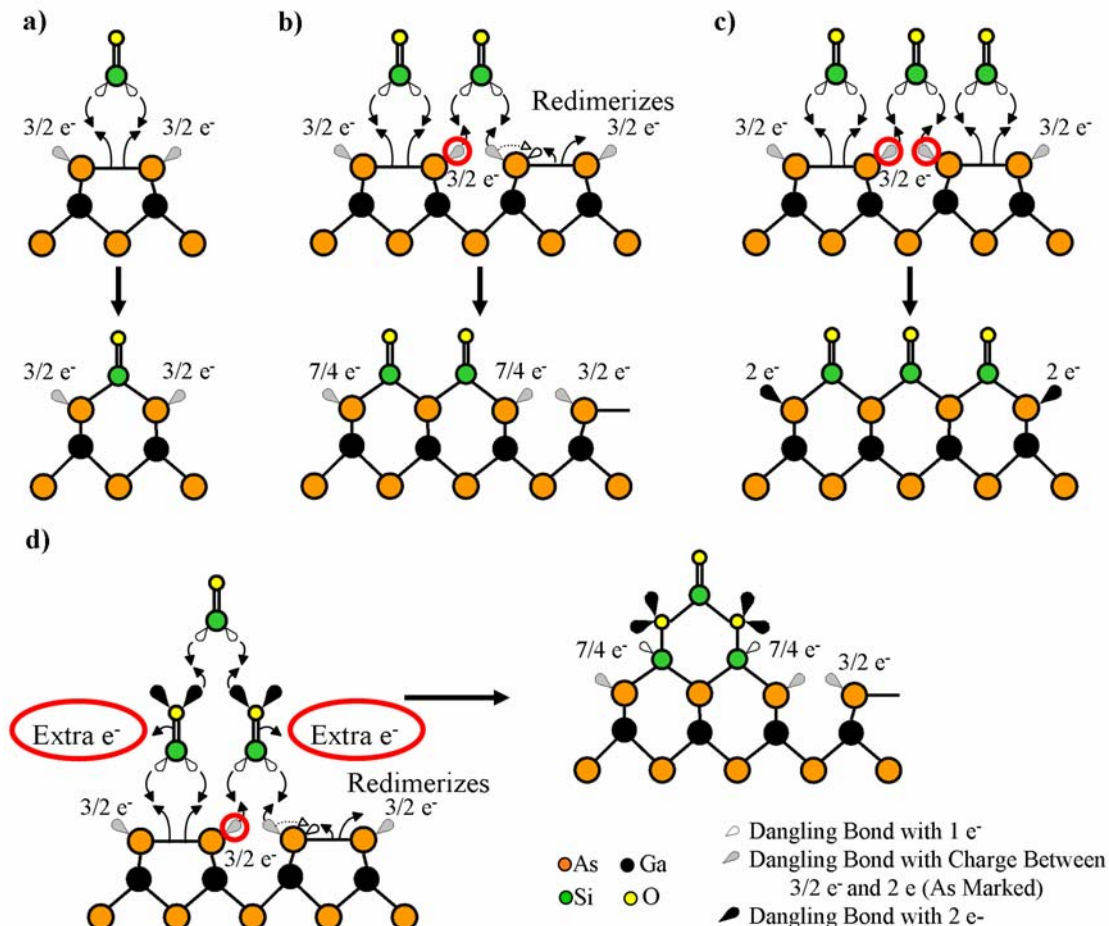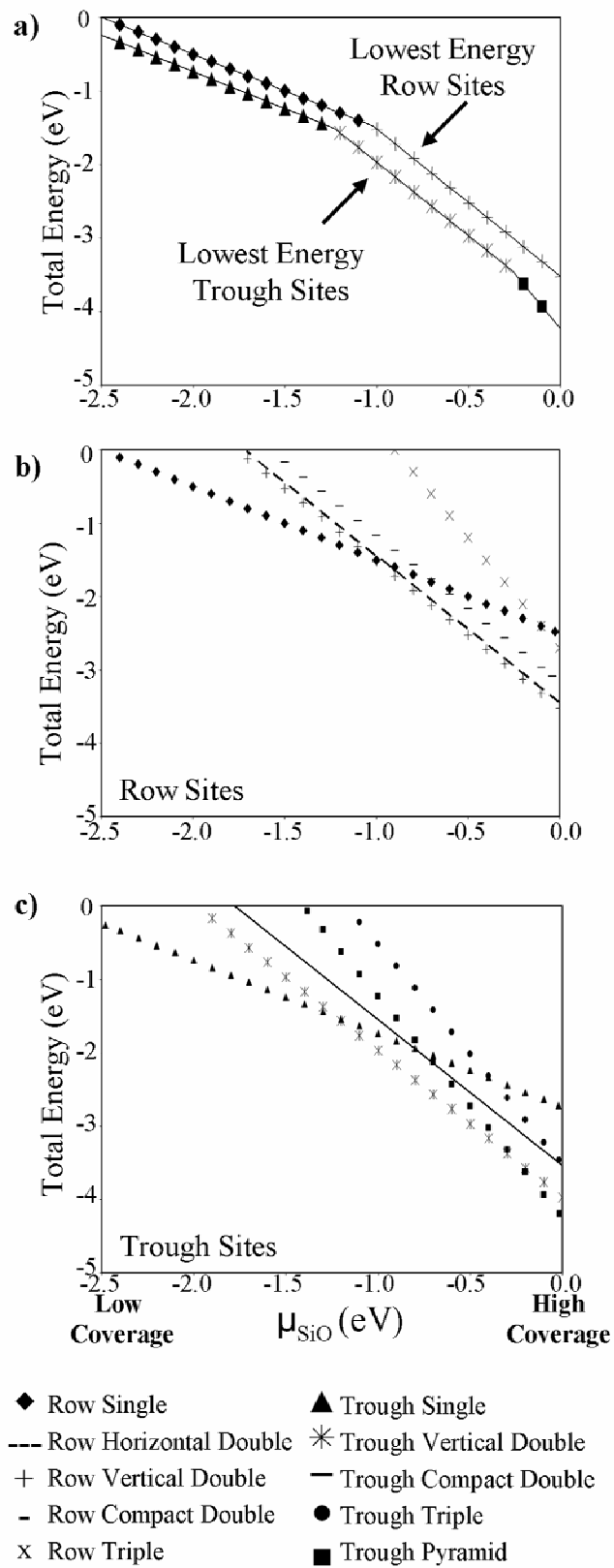
FIGURE 1.4 Ball-and-stick diagrams of proposed SiO/GaAs(001)-(2×4) adsorption configurations before and after bonding. Arrows represent electron relocation during bonding. Prior to bonding the dangling bonds on the As atoms contain a minimum of 3/2 electrons. The electrons noted in the dangling bonds after SiO bonding has occurred are also minimum projected values. All excess electrons caused by SiO bonding are placed in available dangling bonds. Electrons that cause a local buildup of charge are circled in red. (a) Single site, which is predicted to have no charge buildup. (b) Compact double site, which is predicted to have a small amount of charge buildup (~1/2e^-). (c) Triple site, which is predicted to have a greater charge build up than the compact double site (1e^-). (d) Pyramid site, which is predicted to have the same charge buildup as the compact double site, but in addition causes the formation of two partially filled dangling bonds on the bottom two Si atoms.

FIGURE 1.5 The effect of SiO coverage on adsorption site stability is observed in the total energy vs chemical potential plots. As SiO coverage increases, SiO chemical potential likewise increases. (a) A plot of the most stable row and trough sites, which indicates that trough sites are slightly more stable than row sites. (b) A chemical potential plot of solely row sites, showing that the most stable row site changes from the single to the vertical double site as SiO coverage increases. (c) A chemical potential plot of solely trough sites, showing that the lowest energy site changes from the single to the vertical double and finally to the pyramid site as SiO coverage increases.
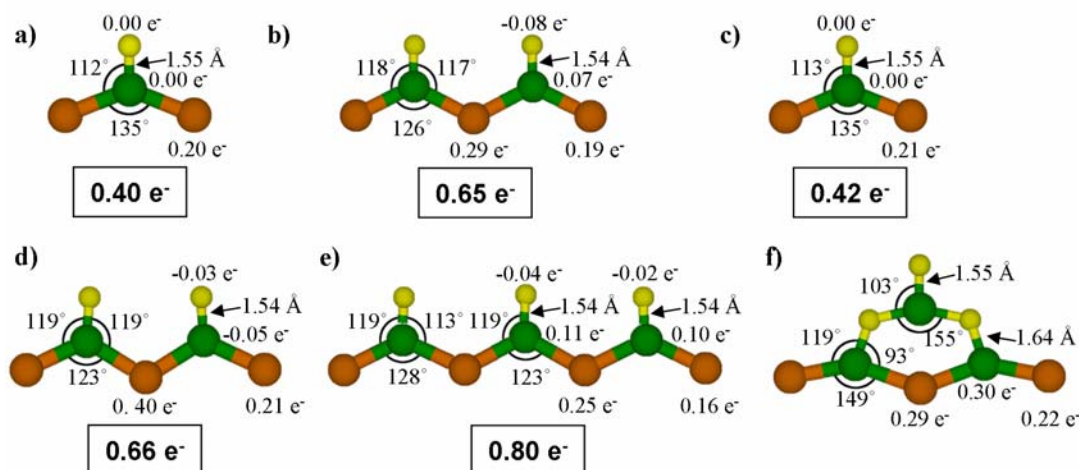
a) Lowest Energy Row Sites

Lowest Energy Trough Sites

b) Row Sites

c) Trough Sites

Low Coverage

High Coverage

μ_{SiO} (eV)

◆ Row Single   ▲ Trough Single

--- Row Horizontal Double   ✳ Trough Vertical Double

+ Row Vertical Double   — Trough Compact Double

– Row Compact Double   ● Trough Triple

x Row Triple   ■ Trough Pyramid

FIGURE 1.6 The bond lengths and bond angles for each calculated SiO structures: (a) row single, (b) row compact double, (c) trough single, (d) trough compact double, (e) trough tripl, and (f) trough pyramid sites. Equivalent bond angles and lengths have been averaged. In addition, relative atomic charges are displayed. The relative charges are the difference between the atomic charge on the clean surface and the surface containing the absorbed SiO molecules. The Si and O relative charges are calculated by comparing the charge on the single sites to the charge on the Si and O atoms in the other sites. In addition the total charge buildup is boxed under each structure. Note that all of the Si atoms (except for those in the trough pyramid site) exhibit bonding angles corresponding to sp^2 hybridization. In addition, charge buildup is smaller on exterior As atoms than on interior atoms.
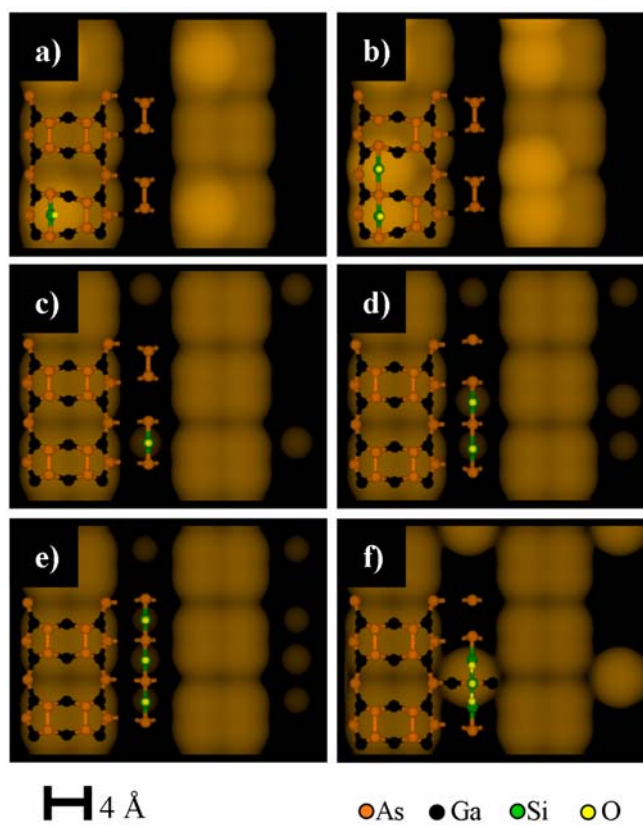
FIGURE 1.7 STM simulations of experimentally observed sites with top-down models of the structures overlaid on the simulations: (a) row single site, (b) row compact double site, (c) trough single site, (d) trough compact double site, (e) trough triple site, and (f) trough pyramid site.
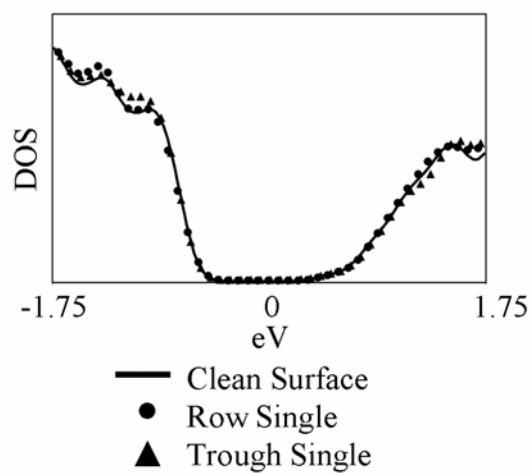
FIGURE 1.8 DFT calculated DOS for the row single site, trough single site, and clean surface. All DOS have been normalized to 1. These simulations show that the row and trough single sites do not cause states to form within the band gap.
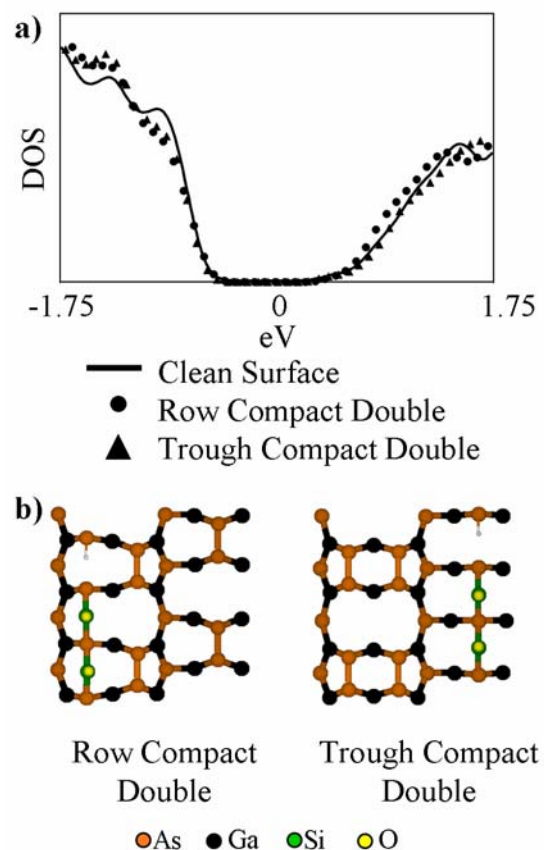
FIGURE 1.9 (a) DOS (normalized to 1) for the row compact double site, trough compact double site, and clean surface. These simulations show that the row and trough compact double sites do not cause states to form within the band gap region. However the band gap is slightly narrower for the row compact double site. (b) Ball-and-stick diagrams of the structures used for the electronic calculation. An H atom is used to passivate the undimerized surface As atom in order to remove the states originating from the undimerized As atom.
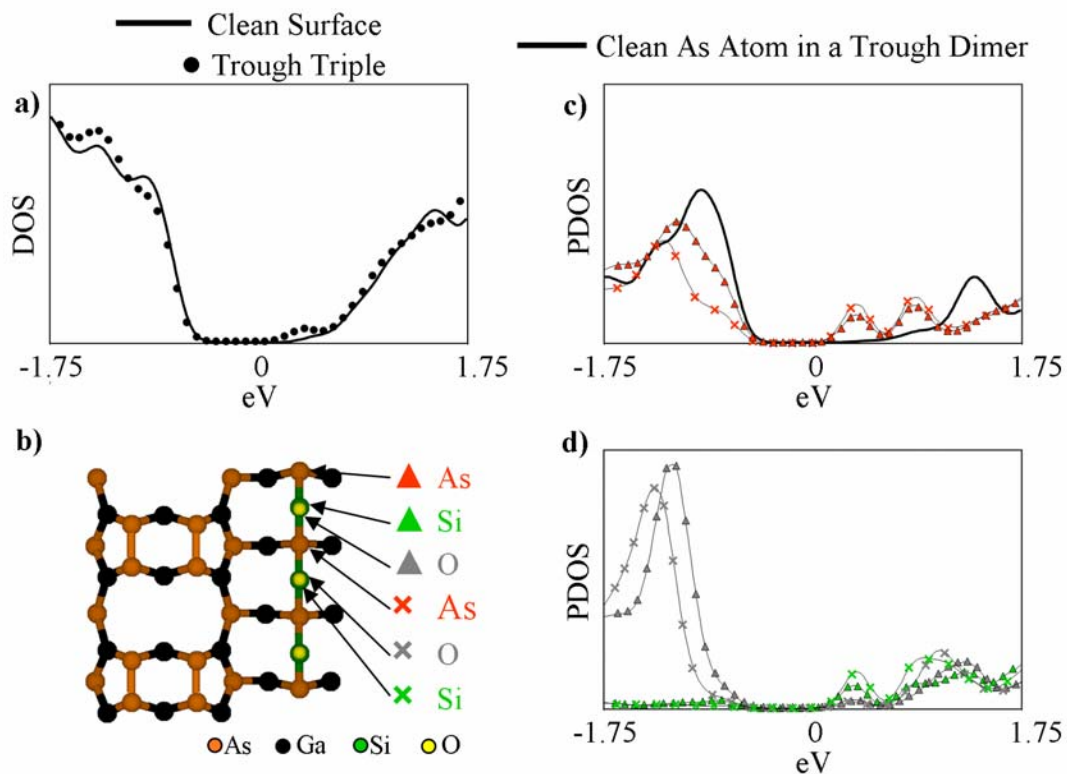
FIGURE 1.10 (a) DOS (normalized to 1) for the clean surface and the surface containing the trough triple site. (b) Top-down model of the trough triple site with the atoms labeled that are seen in the PDOS plots. (c) PDOS of the relevant As atoms; the PDOS of equivalent As atoms have been averaged. All PDOS have been normalized to 1. The As PDOS shows that the trough triple site causes band edge states. (d) PDOS (normalized to 1) of the Si and O atoms; the PDOS of equivalent Si and O atoms have been averaged. Similar to the As PDOS, band edge states also reside on the Si and O atoms.
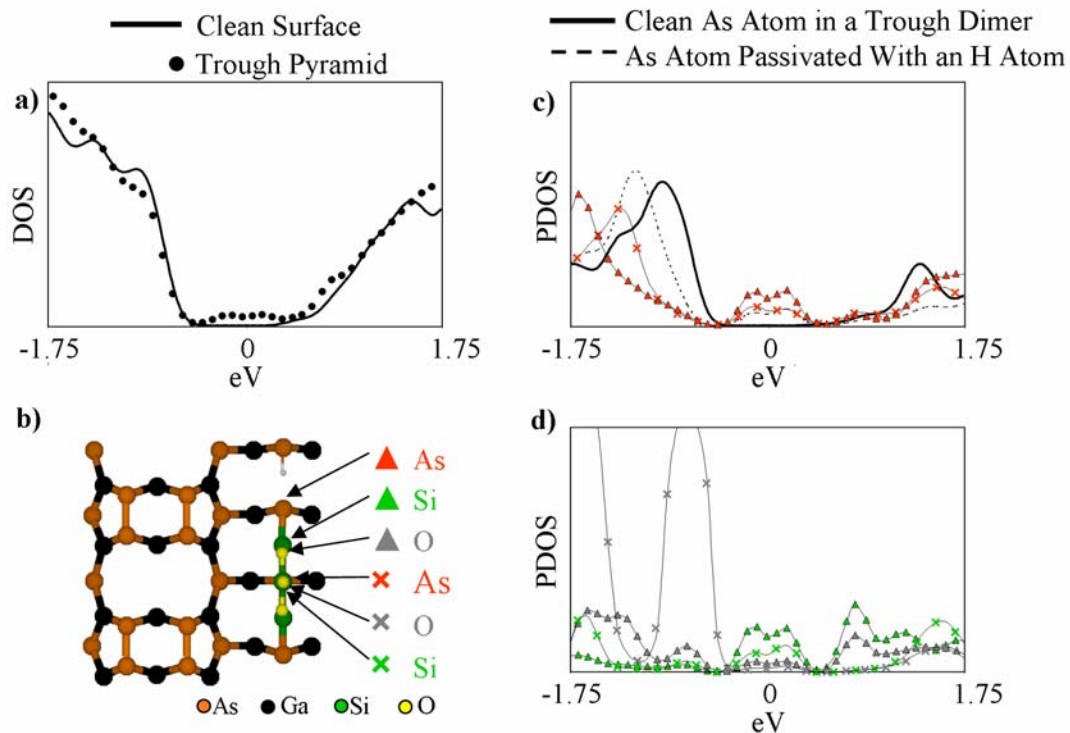
FIGURE 1.11 (a) DOS (normalized to 1) for the clean surface and the surface containing the trough pyramid site. The undimerized As atom has been passivated with a H atom, therefore the states seen are only caused by the pyramid site. (b) Top-down model of the trough pyramid site with the atoms labeled that are seen in the PDOS. (c) PDOS (normalized to 1) of the relevant As atoms. The PDOS of equivalent As atoms have been averaged. The As PDOS shows that the trough triple site causes a state in the middle of the band gap. (d) PDOS (normalized to 1) of the Si and O atoms. The PDOS of equivalent Si and O atoms have been averaged. Similar to the As PDOS, the midgap state is also found to reside on the Si and O atoms.
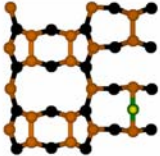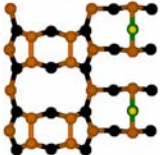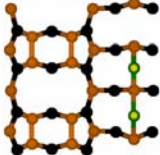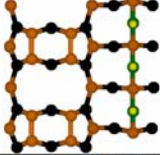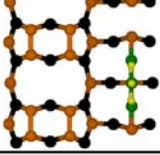
1.8 Tables

TABLE 1.1 Summary of enthalpies of adsorption for row sites, with top-down models. The "ΔH (total)" column displays the enthalpy of reaction for the entire slab. The numbers in this column are divided by the number of SiO molecules per slab and the results are displayed in the "ΔH (per SiO)" column. It is necessary to calculate the "Corrected (per SiO)" values for structures that have an undimerized surface As atom in them. To calculate these corrected values, half of the stabilization energy for an As dimer is added to the ΔH (total) value and the resulting number is then divided by the number of SiO molecules in the slab.

Row Sites	Top Down Cut Away View	ΔH_{ads} (Total)	ΔH_{ads} (Per SiO)	Corrected (Per SiO)
Single		-1.08 eV	-1.08 eV	N/A
Horizontal Double		-2.02 eV	-1.01 eV	N/A
Vertical Double		-2.10 eV	-1.05 eV	N/A
Compact Double		-1.15 eV	-0.58 eV	-0.87 eV
Triple		-1.28 eV	-0.43 eV	N/A

○As ●Ga ○Si ○O

TABLE 1.2 Summary of enthalpies of adsorption for trough sites, with top-down models. The "ΔH (total)" column displays the enthalpy of adsorption for the entire slab. The numbers in this column are divided by the number of SiO molecules per slab and the results are displayed in the "ΔH (per SiO)" column. It is necessary to calculate the "Corrected (per SiO)" values for structures that have an undimerized surface As atom in them. To calculate the corrected values, half of the stabilization energy for an As dimer is added to the ΔH (total) value and the resulting number is then divided by the number of SiO molecules in the slab.

Trough Sites	Top Down Cut Away View	ΔH_{ads} (Total)	ΔH_{ads} (Per SiO)	Corrected (Per SiO)
Single		-1.32 eV	-1.32 eV	N/A
Vertical Double		-2.55 eV	-1.28 eV	N/A
Compact Double		-1.59 eV	-0.80 eV	-1.06 eV
Triple		-2.10 eV	-0.70 eV	N/A
Pyramid		-2.28 eV	-0.76 eV	-0.94 eV

○As ●Ga ●Si ○O

1.9 Acknowledgments

This chapter has been published:

The dissertation author was the primary author and researcher of this paper.

CHAPTER TWO

Electronic Properties of Adsorbates on
GaAs(001)-*c*(2×8)/(2×4)

2.1 Abstract

A systematic experimental and theoretical study was performed to determine the causes of oxide-induced Fermi level pinning and unpinning on GaAs(001). Scanning tunneling spectroscopy (STS) and density functional theory (DFT) were used to study four different adsorbates' (O_2, In_2O, Ga_2O, and SiO) bonding to the GaAs(001)-*c*(2×8)/(2×4) surface. The STS results revealed that out of the four adsorbates studied, only one left the Fermi level unpinned, Ga_2O. DFT calculations were used to elucidate the causes of the Fermi level pinning. Two distinct pinning mechanisms were identified: direct (adsorbate-induced states in the band gap region) and indirect pinning (generation of undimerized As atoms). For O_2 dissociative chemisorption onto GaAs(001)-*c*(2×8)/(2×4), the Fermi level pinning was only indirect, while direct Fermi level pinning was observed when In_2O was deposited on GaAs(001)-*c*(2×8)/(2×4). In the case of SiO on GaAs(001)-*c*(2×8)/(2×4), the Fermi level pinning was a combination of the two mechanisms.

2.2 Introduction

Over the last three decades multiple successful/unsuccessful attempts have been made to construct a GaAs-based metal-oxide-semiconductor field effect transistor (MOSFET) device.[3-10] A GaAs-based MOSFET could potentially provide lower leakage current and lower standby power than current GaAs metal-semiconductor field effect transistors and high electron mobility transistors. In order to develop a GaAs-based MOSFET device with the best possible device characteristics, it is important to understand and characterize the oxide/GaAs interface at the molecular level. Having a molecular understanding of the interface facilitates the selection of the best oxide for a GaAs-based MOSFET device.

Previous studies using scanning tunneling microscopy (STM) performed by Kruse *et al.*,[67] Hale *et al.*,[29,30] and Winn *et al.*[68] have detailed the bonding geometries of O_2, In_2O, Ga_2O, and SiO on the GaAs(001)-c(2×8)/(2×4) surfaces. Although complete STM studies of the bonding sites have been performed, only limited information is available on the electronic properties of these systems. Looking at a wide range of oxides allows more general conclusions to be drawn on the causes of Fermi level pinning of GaAs(001)-c(2×8)/(2×4).

Using the previously determined bonding sites,[29,30,67,68] density functional theory (DFT) calculations were performed to help explain the experimental scanning tunneling spectroscopy (STS) results. The experimental STS studies showed that

Ga$_2$O left the Fermi level unpinned while O$_2$, In$_2$O, and SiO pinned the Fermi level. The Fermi level pinning was attributed to direct and/or indirect mechanisms.

2.3 Experimental and Computational Techniques

The experiments were performed in an UHV chamber with a base pressure of 3×10^{-10} Torr. The chamber was equipped with low energy electron diffraction (LEED), and a Park Scientific VP STM with STS capabilities. As$_2$ capped *n*- and *p*-type GaAs wafers with Si and Be dopant concentrations of 2×10^{-17} cm^{-3} were used for the Ga$_2$O and SiO experiments. For the O$_2$ and In$_2$O studies, wafers with dopant concentration of 2×10^{-16} cm^{-3} were employed. The wafers were thermally decapped to the GaAs(001)-*c*(2×8)/(4×2) reconstruction by performing annealing cycles to 420ºC. Cycles were continued until no pressure rise was observed during the ramp (typically 20 cycles). Details of the decapping procedure have been discussed elsewhere.[68] The surface periodicity was then verified by employing both LEED and STM. Variable tip-sample separation differential conductance (dI/dV) measurements were taken to confirm that the clean surface was unpinned. Subsequently O$_2$, In$_2$O, Ga$_2$O, or SiO were deposited onto the surface. An effusion cell was used to deposit the In$_2$O, Ga$_2$O and SiO, while a UHV leak valve was employed for the O$_2$. Details of the deposition and dosing procedures are discussed elsewhere.[29,30,67,68] After deposition, the

electronic properties of the system were evaluated using STS. STS measurements were taken by employing the variable tip-sample separation method developed by Feenstra.[37-39]

DFT calculations were performed using the Vienna *ab initio* simulation package (VASP).[51-54] The adsorbate/surface systems were modeled using an eight layer GaAs(001) slab that was bottom-terminated with H atoms having a $1.25e^-$ configuration. The bottom three layers of the slab, along with the H atoms were frozen in bulk position to preserve the bulk properties of the system. These calculations were performed using the Perdew-Burke-Ernzerhof (PBE)[55] variation of the generalized gradient approximation. Atoms were modeled using projector augmented wave (PAW) potentials.[56,69] The plane wave cut off energy was set to 400 eV and a $4\times4\times1$ Monkhorst-Pack[58] k-point sampling scheme was used, which resulted in the generation of four irreducible k-points in the first Brillouin zone. The structures were considered fully relaxed when the interatomic forces were below 0.01 eV/Å. The calculations were assumed to be accurate within 0.10 eV; a more in-depth discussion on how the ±0.10 eV error value was reached is presented elsewhere.[68]

2.4 Results and Discussion

A.   Bonding sites and enthalpies of adsorption

All of the systems of interest have their bonding geometries well documented in literature.[29,30,67,68] Previous calculations performed on these systems could not be compared due to a lack of consistency in the computational methodologies. Figures 1 - 4 show top-down views of the experimentally observed sites for O, In_2O, Ga_2O, and SiO; in addition, the enthalpies of adsorption per molecule are displayed. The structures that incorporate an undimerized As atom in them (O single dimer displacements, SiO row compact double, SiO trough compact double, and SiO trough pyramid sites) have had their energies corrected by adding half the energy of an As dimer for every undimerized As atom in the calculation.

1. O_2 dissociative chemisorption

The DFT models of the two experimentally observed O sites are seen in Fig. 1. These sites include the single dimer displacement and the double dimer displacement sites. In these sites, either one or two O_2 molecules adsorb onto the surface and displace row As atoms that are adjacent to each other. This process generates excess As atoms on the surface. From the enthalpies of adsorption, it can be seen that the double dimer displacement [Fig. 1(b)] is only slightly more favorable (by 0.35 eV/O) than the single dimer displacement [Fig. 1(a)]. Kruse *et al.*[67] experimentally showed that when GaAs(001)-*c*(2×8)/(2×4) is exposed to O_2, the surface contains a mixture of the two sites. One critical difference exists between the two sites; the single dimer

displacement causes the formation of two undimerized As atoms, while the double dimer displacement site does not.

2. In_2O chemisorption on rows and troughs

Hale *et al.*[29] showed that when In_2O was deposited onto GaAs(001)-$c(2\times8)/(2\times4)$ at 400ºC, even at low coverage, bonding sites formed in both the row and trough regions. At ~1 monolayer (ML) In_2O coverage, the average spacing between In_2O molecules was greater than 24 Å, revealing that the In_2O molecules had no affinity for clustering.

The enthalpies of adsorption of the seven In_2O bonding sites considered in this study are given in Fig. 2. Three of the sites are considered single sites because they only contain one In_2O molecule: row insertion [Fig. 2(a)], trough over dimer [Fig. 2(b)], and trough between dimer [Fig. 2(c)] sites. The insertion site occurs when an In_2O molecule inserts into a row As dimer. The trough sites occur when an In_2O molecule forms a bridge bond across the trough; the In_2O molecules can be positioned over the trough As dimers [trough over dimer site, Fig. 2(b)] or it can be positioned between two trough As dimers [trough between dimer site, Fig. 2(c)].

The sites remaining are combination sites and are formed by combining multiple single sites: row full coverage insertion [Fig. 2(d)], trough full coverage over dimers [Fig. 2(e)], trough triple [Fig. 2(f)], and complete coverage [Fig. 2(g)] sites. The adsorption energies of the combination sites show that clustering of In_2O molecules has no effect on the adsorption energy. Therefore, only three sites need to

be considered when discussing adsorption energies: row insertion, trough over dimer, and trough between dimer sites.

The adsorption energies of the three single sites show that the row insertion and trough over dimer sites are energetically degenerate within the error range of these calculations. These results are consistent with experimental findings that both row and trough sites form even at low coverage. The trough between dimer site is ~0.29 eV less stable than the row insertion and trough over dimer sites. Therefore, it is expected that the row insertion and trough over dimer sites will fill in before the trough between dimer sites start forming.

Hale *et al.* suggested that the In_2O molecules might be able to bond both O end up and down in the trough region.[29] Multiple attempts were made to find stable structures for the trough over dimer and trough between dimer sites that had O atoms bonded downward into the trough. While no truly stable bonding geometries were found for these configurations, a weak metastable structure was found for the O down trough between dimer site. In order for the In_2O molecule to bond O down between trough dimers, it was necessary to have two other In_2O molecules bonded O end up over adjacent trough dimers, to prevent the In_2O molecule from flipping over in order to orient the O upwards. The adsorption energy for solely the "trapped" O down trough between dimer site was found to be only -0.57 eV. Therefore, it is not clear what role, if any, this site plays in the finial bonding geometry picture.

The In_2O adsorption energies show that it is always energetically preferable to have an In_2O molecule bonded over a trough dimer than between trough dimers. This

difference in energy is most likely a result from interactions between the filled

dangling bonds on the As trough dimers and the oxide molecule. The interaction is

more severe in the between dimer site since the majority of the electron density in the

filled dangling bonds is located in this position.

3. Ga$_2$O chemisorption on rows and troughs

Although one might predict that Ga$_2$O bonding on GaAs(001)-*c*(2×8)/(2×4)

would be similar to In$_2$O bonding to GaAs(001)-*c*(2×8)/(2×4), there are actually major

differences between these two isoelectronic systems. The STM images taken by Hale

et al.[30] of Ga$_2$O deposited onto GaAs(001)-*c*(2×8)/(2×4) showed that the initial

bonding site for the Ga$_2$O molecules was to insert into the row As dimers. Unlike

In$_2$O, no low coverage trough sites were ever experimentally observed.

The high coverage results for Ga$_2$O were also distinctly different than those for

In$_2$O. At high coverage (~1 ML), the Ga$_2$O molecules were found to form parallel

rows on the surface with the most common row spacing being ~8 Å. This result

suggests that unlike In$_2$O, Ga$_2$O has an affinity for clustering. The ~8 Å, Ga$_2$O row

spacing yielded a (2×2) surface periodicity. The typical separation between the As

dimer rows on the GaAs(001)-*c*(2×8)/(2×4) surface is ~16 Å. Therefore, in order to

form an ~8 Å row spacing, the surface would need to undergo a surface

reconstruction. Experimentally, it was observed that as the concentration of Ga$_2$O on

the surface increased, the number of steps also increased. It was assumed that this step

formation generated the needed As atoms to allow for the (2×2) reconstruction to

form. Even though the majority of the In_2O molecules were found to have a row spacing of greater than 24 Å, a small number of In_2O molecules were found with a row spacing of ~8 Å. This suggest that small areas of the In_2O surface also might have undergone some rearrangement.[29]

Calculations reveal that the row insertion site [Fig. 3(a)] is -1.87 eV exothermic, consistent with the low coverage experimental results. In addition, the adsorption energies of two trough sites were calculated for comparison with In_2O bonding sites. Although the trough sites were not observed with STM, the stability of the trough over dimer and trough between dimer sites (-1.06 and -0.69 eV, respectively) indicate that the trough filling mechanism is probably more complex than a simple As rearrangement.

Calculations were also attempted on a Ga_2O down trough sites but no stable/metastable sites were found. This was attributed to the fact that the Ga_2O molecules are slightly smaller than the In_2O molecules, which enables them to rotate into the energetically preferred position of O up, regardless of the surrounding environment.

In an effort to understand the energy discrepancy between the trough and row sites, an in-depth look must be taken at the fundamental bonding properties of the systems. On GaAs(001)-(2×4), when the Ga_2O inserts into the row, Ga-As bonds are created; conversely when Ga_2O bonds in the trough, Ga-Ga bonds are created. In covalent compounds, Ga-Ga bonds are ~1/2 as stable as Ga-As bonds.[70] The other major difference between the row and trough sites is that four bonds are created when

each row insertion site is formed and only two bonds are created when either of the two trough sites are formed.

Not only is it important to understand what bonding sites will be occupied, it is equally important to understand energetic differences between the In_2O and Ga_2O bonding sites on the GaAs(001)-c(2×8)/(2×4) surface. The Ga_2O trough site energies are comparable to the In_2O trough sites energies. However, the Ga_2O row insertion site is significantly more stable than the In_2O row insertion site (-1.87 eV vs. -1.18 eV, respectively). The difference in stability between the row insertion sites results from Ga-As and In-As bond strength differences. In order to estimate the approximate bond strength difference of Ga-As and In-As bonds, the enthalpies of reaction were calculated for the following two reactions using VASP.

$$Ga_2OAs_4H_8+2H_2 \rightarrow Ga_2O+4AsH_3 \qquad (1)$$

$$In_2OAs_4H_8+2H_2 \rightarrow In_2O+4AsH_3 \qquad (2)$$
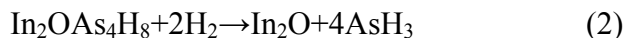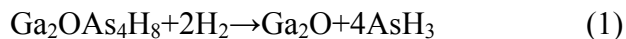
The difference in enthalpies of reaction is equal to four times the difference in bond energies between Ga-As and In-As bonds; this was calculated to be 0.57 eV. This value is comparable to the Ga_2O and In_2O insertion site energy differences (0.69 eV). Therefore, it can be concluded that the main difference between these two systems arises from the bond strengths.

4. SiO chemisoption on rows and troughs

Six bonding sites are experimentally observed at low coverage for SiO deposited on GaAs(001)-c(2×8)/(2×4) [Fig. 4]. These sites include row and trough

single [Figs. 4(a) and 4(b), respectively], row and trough compact double [Figs. 4(c) and 4(d), respectively], trough triple [Fig. 4(e)], and trough pyramid [Fig. 4(f)] sites. The row and trough single sites form when a SiO molecule inserts into an As-As dimer bond in either the row or trough. If an additional SiO molecule inserts between a single site and an adjacent dimer then the site is referred to as a row or trough compact double site. There are two more complex bonding geometries that are only found in the trough region: trough triple and trough pyramid sites. The trough triple site forms when two trough single sites bond in adjacent dimers and an additional SiO molecule bonds between the two occupied dimers. In order for a trough pyramid site to form, a trough compact double site forms, and subsequently, an additional SiO molecule bonds on top, forming a pyramid. A detailed investigation of these bonding sites along with a chemical potential plot showing that all of these geometries are viable bonding sites, depending on the SiO coverage, is presented elsewhere.[68] The trough sites were found to be slightly more favorable than their row counterparts. This was attributed to stabilization received from the dangling bonds of the Ga atoms that protrude into the trough. In addition, the stabilization received from the dangling bonds of the Ga atoms allows the more complex sites (trough triple and trough pyramid sites) to form in the trough region.

B.   Scanning tunneling spectroscopy and density of states measurements

Surface electronic measurements were taken of the different systems using STS. For all STS measurements, the Fermi level resides at 0 V. Figure 5(a) shows $(dI/dV)/(\overline{I/V})$ vs. V measurements, which are proportional to the surface density of states (DOS), of the clean *n*- and *p*-type surfaces.[71] The Fermi level resides near the conduction band for the clean, oxide-free *n*-type surface and resides near the valence band for the clean oxide-free *p*-type surface, typical of an unpinned surface.

DOS calculations were also performed on the clean surface [Fig. 5(b)], as well as the oxide covered surfaces. These calculations differ from STS measurements in two major ways. First, the computational slabs are not large enough to be doped; therefore, the computational slabs are intrinsic. Second, the position of the Fermi level within the band gap is somewhat arbitrary in DFT; therefore, in all the DFT calculations the DOS have been aligned using the deep level states. Regardless of these differences, if the calculated DOS shows adsorbate induced states within the band gap region, it can be reasonably concluded that the adsorbate would cause the experimental surface to be pinned.

1. O₂ chemisorbate electronic structure

Figure 6(a) shows a STS measurement of *n*-type sample after ~900 L exposure to O_2. The conduction band is not observed for this *n*-type sample due to the low dopant concentration of the wafer, which prohibits complete inversion from being

obtained during the STS measurment.[72]   The STS measurement reveals that the

bands have bent causing the Fermi level to be located midgap (~0.7 V from the

valence band edge); this is typical of a pinned sample.   Although no *p*-type STS

spectra are presented in this paper, other groups have verified that exposing O_2 to

GaAs pins the Fermi level.[12,13]

To deduce the cause of the Fermi level pinning seen experimentally, DOS and

projected density of states (PDOS) calculations were performed. Figure 6(b) presents

the calculated DOS for a surface containing two O atoms that have replaced two As

atoms, and a surface containing four O atoms that have replaced four As atoms. The

DOS of the clean surface is also displayed for comparison. The plots reveal that states

are only generated in the band gap region when two O atoms replace two As atoms.

To further investigate which atoms contribute to the states in the DOS, PDOS

calculations were performed. PDOS calculations for the surface As atoms are seen in

Fig. 6(c). The PDOS reveals that the major contributors to the midgap states are the

undimerized As atoms. This also rationalizes why no states are observed in the band

gap region when four O atoms replace four As atoms, because no undimerized As

atoms are generated. This suggests that the properties of the O atoms do not directly

cause Fermi level pinning on the GaAs(001)-*c*(2×8)/(2×4) surface; instead, the

pinning is most likely due to the generation of undimerized As atoms. Therefore, the

pinning mechanism is considered to be indirect.   Previous reports incorrectly

attributed the pinning to a direct mechanism but this was due to inferior or incorrect

computational methods.[30]

On real (experimental) surfaces, the undimerized As atoms may be able to redimerize, thereby eliminating the midgap As states, if two criteria are met. First, the activation barrier must be low enough to allow for the reconstruction of the row, in order to facilitate the redimerization of the As atoms. Second, there must be another undimerized As atom in the same row to terminate the process with a complete dimer. Although it might be possible to meet both of these constraints, the second criteria becomes harder to fulfill on smaller terraces. If these criteria cannot be met, and undimerized As atoms remain on the surface, the Femi level is expected to be pinned.

H atoms can be used to (computationally) passivate these undimerized As atoms in order to verify that they are the only cause of O induced states. Figure 6(d) displays the DOS for a surface containing two O atoms and two undimerized As atoms, and a surface containing two O atoms with the undimerized As atoms passivated with H atoms. The plot clearly shows that the H passivation suppresses the states in the band gap region, yielding a DOS that is similar to the clean unpinned surface. This result indicates that it is the resultant dangling bonds on the undimerized As atoms that causes the observed Fermi level pinning. This result also indicates that H passivation can be used for any system that has undimerized As atoms; once the H atoms have been used to passivate the undimerized As atoms, any states left in the band gap region are a direct result of the adsorbate bonding with the surface.

2. In$_2$O chemisobate electronic structure

STS results of In$_2$O on GaAs(001)-c(2×8)/(2×4) are presented in Fig. 7(a). Although the n-type sample has the same STS spectra as the unpinned surface, the p-type sample clearly shows that the In$_2$O deposited on GaAs(001)-c(2×8)/(2×4) causes the Fermi level to be pinned near the conduction band edge.

The DOS of the In$_2$O single sites (row insertion, trough over dimer, and trough between dimer) in Fig. 7(b) shows that none of these sites induce states in the band gap region. Although the single sites do not cause state formation in the band gap, all of the combination sites (row full coverage insertion, trough full coverage over dimers, trough triple, and complete coverage) induce states into the band gap region, as shown in Fig. 7(c). As the coverage on the row increases from the row insertion site to the full coverage insertion site, state formation is seen in the band gap region. Similarly, as the trough coverage increases form the single trough sites to the trough full coverage over dimer site, and finally to the trough triple site the state density in the band gap region also increases. These results suggest that the higher the In$_2$O coverage, the greater the state formation in the band gap. This was further substantiated by the DOS for the experimentally observed high coverage site (complete coverage in which every available site is filled), which has the highest state formation in the band gap region of all the sites. A PDOS analysis revealed that the pinning states were delocalized and existed throughout the top four layers of the slab.

Hale *et al.* reported that room temperature deposition resulted in In$_2$O molecules inserting into missing As row dimers (defect sites).[29] Calculations were performed on this geometry and the site was shown to only be marginally stable (-0.33

eV). The DOS revealed that these empty dimer sites generated states in the band gap. However, it is not believed that this site plays a major role in the Fermi level pinning since the concentration of these sites is very low.

In_2O pinning is distinct from pinning by the other oxides (O_2 and SiO) on GaAs(001)-c(2×8)/(2×4) because In_2O experimentally pins the Fermi level near the conduction band edge while the other oxides experimentally pin the Fermi level midgap. Although states generated in the band gap region are distinctly different depending on whether multiple row or multiple trough sites caused the formation, both types of states can be evaluated to understand why In_2O pins the Fermi level near the conduction band. Multiple row insertion sites induce states that start at the valence band edge and extend toward the conduction band, residing in over half of the band gap region. Analysis of the Kohn-Sham orbital occupancies indicates that these are filled states. These results imply that the Fermi level should indeed be pinned near the conduction band edged inside the reduced band gap. The states that are generated when the coverage increases and multiple trough sites are forced to form in close proximity to each other are located at both the valence and conduction band edges. Although it is clear that these states play a role in the Fermi level pinning, it is difficult to conclude exactly where the Fermi level should reside as a result.

3. Ga_2O chemisorbate electronic structure

Experimental and calculated electronic structures of Ga_2O on GaAs(001)-c(2×8)/(2×4) are displayed in Fig. 8. STS measurements [Fig. 8(a)] show that the

Fermi level resides close to the conduction band for *n*-type samples and close to the valence band for *p*-type samples, revealing that Ga_2O leaves the GaAs(001)-c(2×8)/(2×4) surface unpinned. These findings were further substantiated by the fact that the calculated DOS [Fig. 8(b)] for the insertion site had no states in the band gap region. The DOS for the trough over dimer and trough between dimer sites are also displayed in Fig. 8(b), for comparison with the In_2O system. Although these sites are not explicitly seen experimentally, the DOS reveals that both the Ga_2O trough between dimer and trough over dimer sites also have no states in the band gap region.

The Ga_2O insertion site leaves the Fermi level unpinned because the insertion site does not trigger any chemical event which causes Fermi level pinning. In contrast to O_2 chemisorption on the GaAs(001)-c(2×8)/(2×4) surface, the Ga_2O insertion site does not cause the generation of undimerized As atoms nor does it cause the generation of excess As atoms. In addition, when a Ga_2O molecule bonds on the row, the filled dangling bonds on the row As atoms are preserved, and no extra dangling bonds are introduced.

The electronic effects of increased coverage were also computationally explored for Ga_2O on GaAs(001)-(2×4). Similar to In_2O all of the higher coverage Ga_2O sites pinned the Fermi level. However, the simulated high coverage sites for Ga_2O do not represent the experimental surface since they do not result in a (2×2) surface reconstruction. Therefore, these results are not relevant to the examination of the electronic properties of Ga_2O on GaAs(001)-c(2×8)/(2×4).

Calculations were also performed for a Ga_2O molecule inserting into a missing As row dimer. Similar to the In_2O case this site was also found to induce states into the band gap region. In addition, the bonding geometry was found to be significantly more stable for Ga_2O than for In_2O (-0.42 eV more stable). Therefore, since Ga_2O was experimentally shown to leave the Fermi level unpinned the number of defect sites must be small enough to not play a major role in the electronic properties of the system.

4. SiO chemisorbate electronic structure

STS of SiO on GaAs(001)-*c*(2×8)/(2×4) is presented in Fig. 9(a). The STS results reveal that SiO deposition on GaAs experimentally pins the Fermi level at midgap. The calculated DOS for the row and trough adsorption sites are seen in Figs. 9(b) and 9(c), respectively. The DOS have H atoms passivating any undimerized As atoms that were generated by the bonding sites, leaving only the states directly induced by the SiO molecules. These DOS show that only two of the six geometries (trough triple and pyramid sites) directly induce states in the band gap region. These results are consistent with the experimental findings. In addition, the compact double sites and the pyramid site generate undimerized As atoms, which most likely play an indirect role in the Fermi level pinning.

PDOS analysis was performed on the trough triple [Fig. 9(d)] and trough pyramid [Fig. 9(e)] sites to deduce the causes of state formation in the band gap region for SiO bonded to the GaAs(001)-*c*(2×8)/(2×4) surface. The PDOS from the trough

triple site [Fig. 9(d)] shows that the states observed near the conduction band edge in the DOS reside on the surface As, Si, and O atoms. A Bader style atomic charge analysis[62] revealed that the likely cause of the band gap states in the trough triple site was from a local buildup of charge on multiple adjacent As atoms. Similar to the PDOS of the trough triple site, the trough pyramid site PDOS [Fig. 9(e)] reveals that the band gap states also reside on the surface As, Si, and O atoms. The band gap states were attributed to the generation of partially filled dangling bonds on the bottom Si atoms of the trough pyramid site. A more in-depth study of the SiO/GaAs(001)-$c(2\times8)/(2\times4)$ surface is presented elsewhere.[68]

2.5 Conclusion

Experimental results revealed that out of the four adsorbates studies (O_2, In_2O, Ga_2O, and SiO) only one, Ga_2O, left the Fermi level unpinned when it bonded to GaAs(001)-$c(2\times8)/(2\times4)$. DFT simulations were used to explain the different pinning mechanisms for other adsorbates. The mechanisms can be broken down into two general categories: direct and indirect. Direct Fermi level pinning results when the bonding between the adsorbate and the surface directly induces states into the band gap region. In comparison, indirect Fermi level pinning occurs when states are induced in the band gap region because of secondary effects, such as the generation of undimerized As atoms. Since indirect pinning is not caused by the properties of the

adsorbates themselves, it may be possible to create unpinned surfaces using H passivation or even a multilayer of oxide. Adsorbates that cause Fermi level pinning on GaAs(001)-c(2×8)/(2×4) can either exhibit one of the pinning mechanisms [O (indirect) and In$_2$O (direct)] or they can exhibit both of the mechanisms (SiO). In addition, the close correlation between experiment and theory in this study suggests that DFT can be used on other III-V semiconductor systems to predict oxide pinning and unpinning.

2.6 Figures
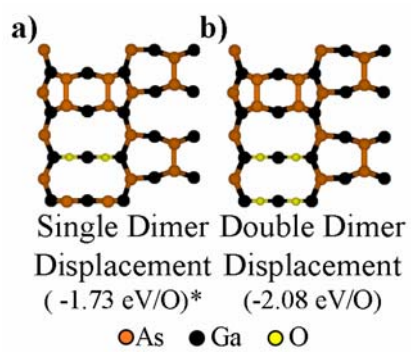
FIGURE 2.1 Top-down views of the lowest energy structures of O_2 bonded to the GaAs(001)-c(2×8)/(2×4) surface: (a) single dimer displacement, and (b) double dimer displacement. The adsorption energy per oxide molecule is displayed below each structure. The energy denoted with "*" has been corrected to include half the As dimerization energy for each undimerized As atom.
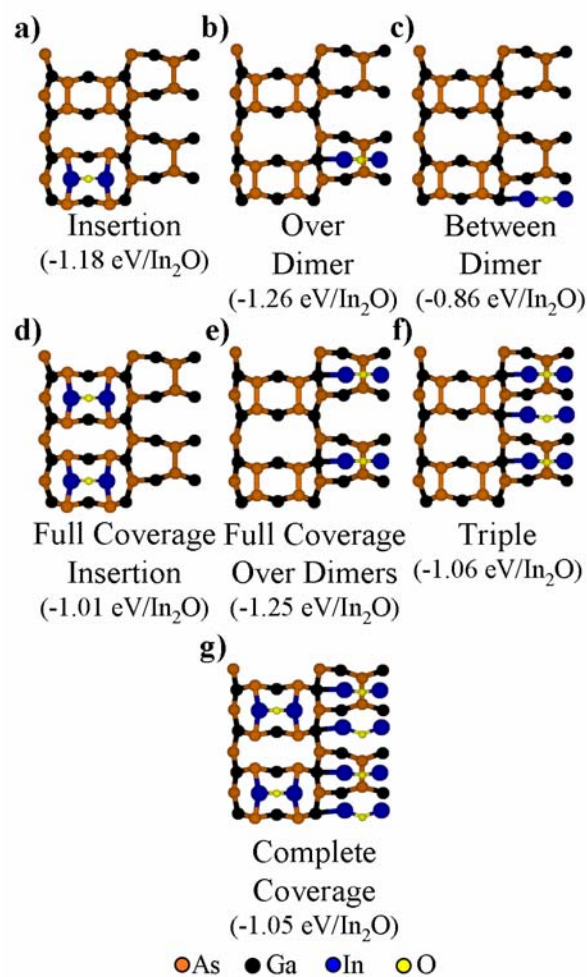
FIGURE 2.2 Top-down views of the lowest energy structures of In$_2$O bonded to the GaAs(001)-c(2×8)/(2×4) surface: (a) row insertion, (b) trough over dimer, (c) trough between dimer, (d) row full coverage insertion, (e) trough full coverage over dimer, (f) trough triple, and (g) complete coverage. The adsorption energy per oxide molecule is displayed below each structures.
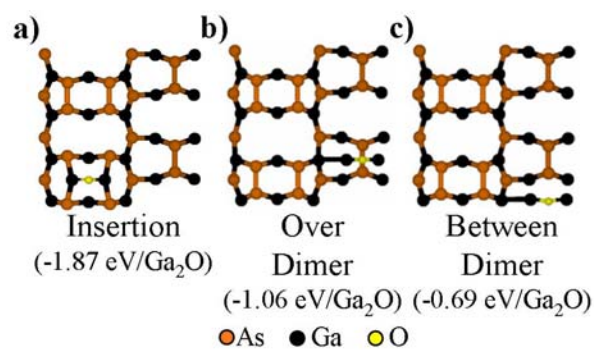
FIGURE 2.3 Top-down views of the lowest energy structures of Ga_2O bonded to the GaAs(001)-c(2×8)/(2×4) surface: (a) row insertion, (b) trough over dimer, and (c) trough between dimer. The adsorption energy per oxide molecule is displayed below each structure.
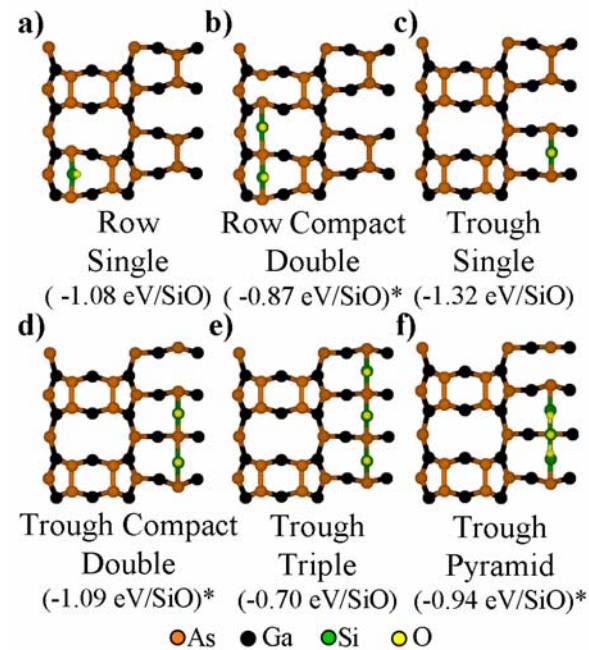
FIGURE 2.4 Top-down views of the lowest energy structures of SiO bonded to the GaAs(001)-c(2×8)/(2×4) surface: (a) row single, (b) row compact double, (c) trough single, (d) trough compact double, (e) trough triple, and (f) trough pyramid. The adsorption energy per oxide molecule is displayed below each structure. The energies denoted with "*" have been corrected to include half the As dimerization energy for each undimerized As atom.
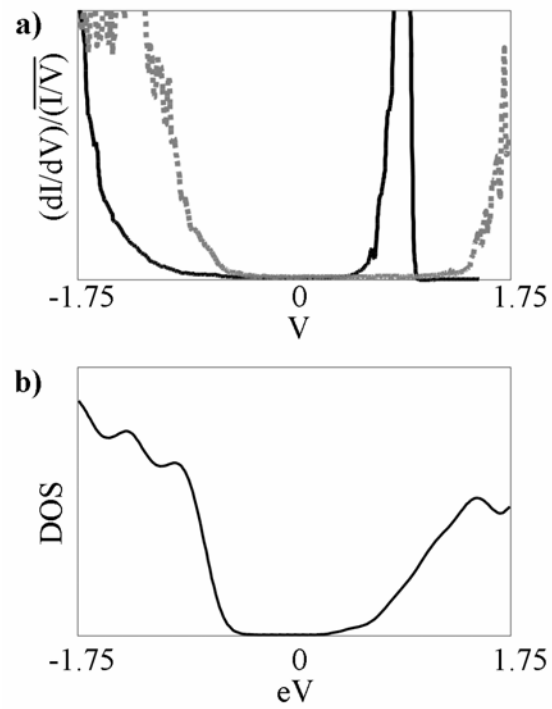
FIGURE 2.5 (a) STS measurements of the clean *n*-type (black solid line) and *p*-type (grey dashed line) GaAs(001)-*c*(2×8)/(2×4) surface. (b) Calculated DOS for the clean surface.
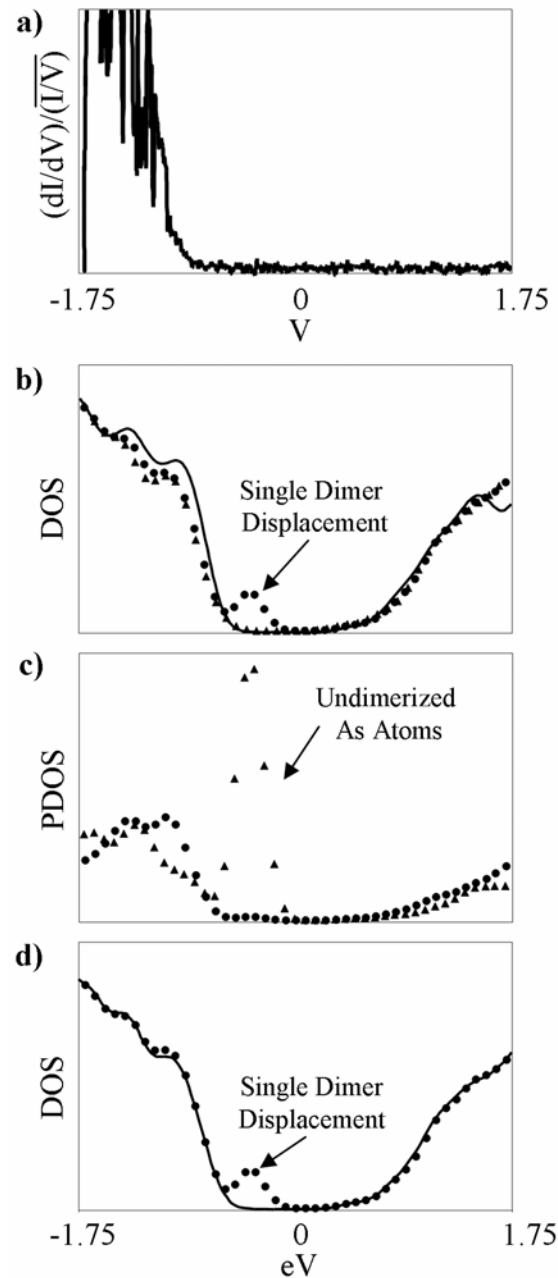
FIGURE 2.6 (a) STS measurement of O_2 adsorbed onto n-type GaAs(001)-$c(2\times8)/(2\times4)$. (b) DOS calculations of O2 sites: clean surface (thick bold line), single dimer displacement ($\bullet$), and double dimer displacement ($\blacktriangle$). (c) PDOS calculations showing the average of the surface As atoms that are dimerized ($\bullet$) vs. the average of the surface As atoms that are not dimerized ($\blacktriangle$). (d) DOS calculations of the unpassivated single dimer displacement ($\bullet$) and the single dimer displacement with the undimerized As atoms passivated with H atoms (thick bold line).
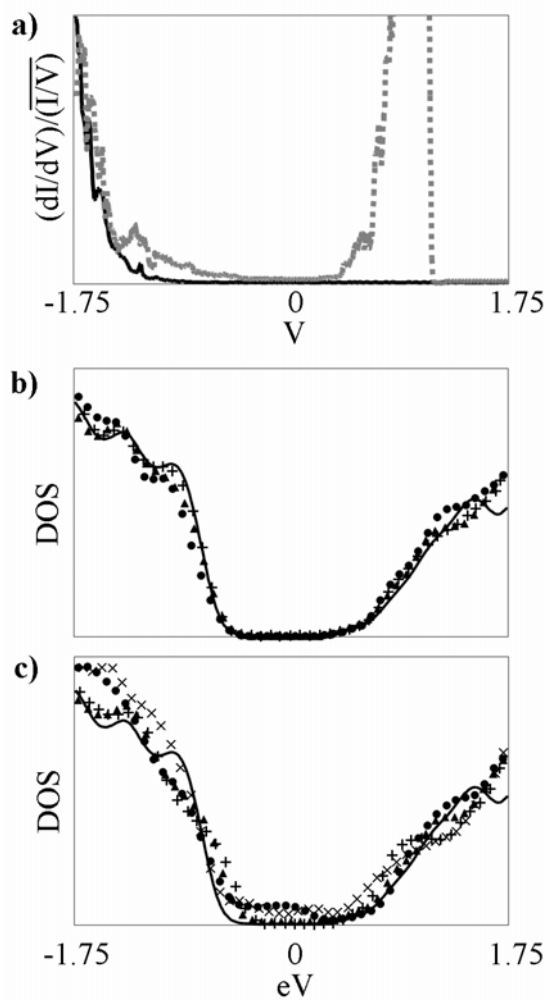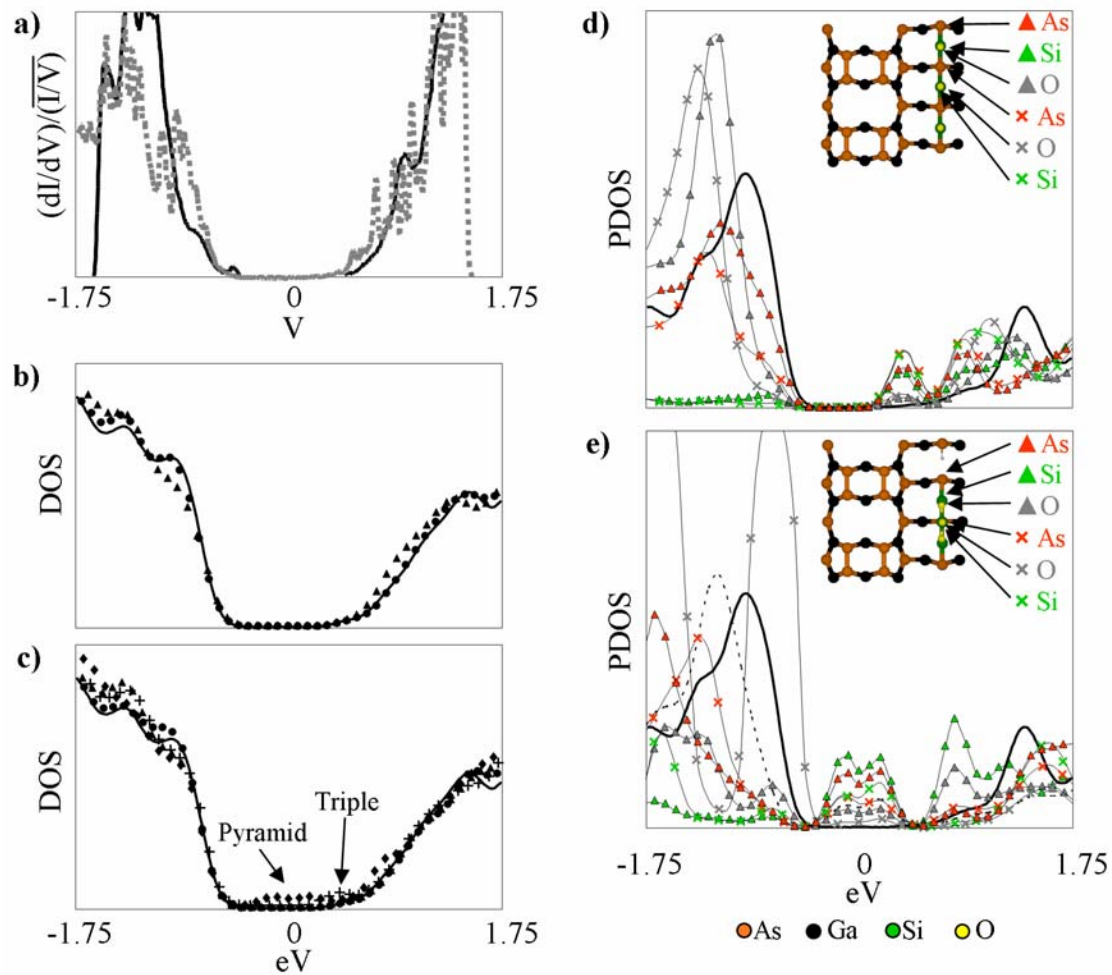
FIGURE 2.7 (a) STS measurements of In_2O adsorbed onto n-type (black line) and p-type (gray dashed line) GaAs(001)-c(2×8)/(2×4). (b) DOS calculations of In_2O sites: clean surface (black line), insertion (●), over dimer (▲), and between dimer (+). (c) DOS calculations of combination sites: row full coverage insertion (●), trough full coverage over dimers (▲), trough triple (+), and complete coverage (×).
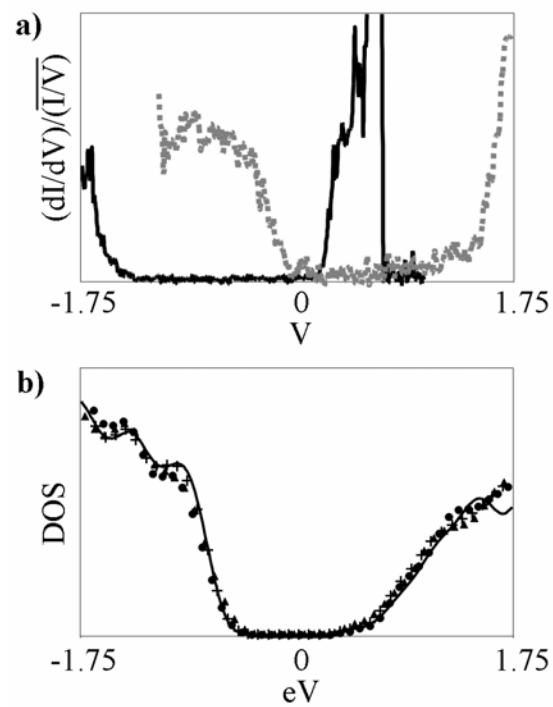
FIGURE 2.8 (a) STS measurements of Ga_2O adsorbed onto n-type (black line) and p-type (gray dashed line) GaAs(001)-c(2×8)/(2×4). (b) DOS calculations of Ga_2O sites: clean surface (thick bold line), row insertion (●), trough over dimer (▲), and trough between dimer (+) sites.

FIGURE 2.9 (a) STS measurements of SiO adsorbed onto *n*-type (black bold line) and *p*-type (grey dashed line) GaAs(001)-*c*(2×8)/(2×4). (b) DOS calculations of the row SiO sites: clean surface (thick bold line), row single (●), and row compact double (▲). (c) DOS of the trough SiO sites: clean surface (thick bold line), trough single (●), trough compact double (▲), trough triple (+), and trough pyramid (♦). (d) PDOS calculations for the trough triple sites, atoms which PDOS have been plotted for are labeled in the ball-and-stick diagram in the upper right hand corner of the plot, the thick black line is a PDOS of a trough As dimer on the clean surface for comparison. (e) PDOS calculations for the trough pyramid sites, atoms which PDOS have been plotted for are labeled in the ball-and-stick diagram in the upper right hand corner of the plot, the thick black line is a PDOS of a trough As dimer on the clean surface and the dashed line is the As atom with the H bonded to it.

2.7 Acknowledgments

This chapter has been submitted for publication:

CHAPTER THREE

Definitive Identification of the InAs(001)-c(8×2)/(4×2) Reconstruction

3.1 Abstract

InAs(001) is well documented to have a (4×2) reconstruction, however, the details of

the reconstruction are still under debate. Atomically resolved filled and empty state

scanning tunneling microscopy (STM) images of the InAs(001)-c(8×2)/(4×2) surface

reveal that the reconstruction is made up of single atom rows that run in the [110]

direction which are separated by ~17 Å. In addition, atomically resolved STM images

show that the row structure is most likely comprised of undimerized atoms. Cl_2 was

deposited onto the surface (which has been shown to preferentially react with III

atoms on III-V semiconductors) to confirm that the rows were in fact comprised of In

atoms. The experimental results suggest that the most probable structure for

InAs(001)-c(8×2)/(4×2) is the undimerized β3(4×2) reconstruction also known as the

β3(4×2)' reconstruction. Density functional theory (DFT) STM simulations were used

to confirm the experimental findings.

3.2 Introduction

Due to InAs's high electron mobility (30,000 $cm^2V^{-1}s^{-1}$) it is a potential channel material candidate for a III-V metal oxide semiconductor field effect transistor (MOSFET) device.[14] An atomic understanding of the oxide semiconductor interface can greatly enhance the electronic properties of the device. Unfortunately, even the clean InAs(001) surface has not been well documented in literature.

Although it is well documented that InAs(001) has a (4×2) surface reconstruction, there is still disagreement about the exact atomic placement of the surface atoms. Since InAs and GaAs have similar chemical properties, it might be assumed that the (4×2) reconstruction of the two semiconductors would be the same. However, scanning tunneling microscopy (STM) images of the two surfaces differ dramatically. Despite the differences in STM images between InAs(001)-(4×2) and GaAs(001)-(4×2), some groups still propose that the InAs structure is the same ζ(4×2)[73,74] reconstruction that has been well documented for GaAs. Other groups have proposed different (4×2) structures that include the α(4×2)[75], β2(4×2)[76], and β3(4×2).[77,78] These structures along with four other possible (4×2) reconstructions [α2(4×2), α3(4×2), β(4×2), and S(4×2)] are seen in Fig. 1. Although numerous papers have attempted to determine the InAs(001)-(4×2) reconstruction, the majority of the papers focused either on experimental determination[75,77,78] or computational determination[73,74,76] of the surface but do not employ both techniques.

Experimental and computational studies were employed for this paper to help determine the InAs(001)-c(8×2)/(4×2) reconstruction. Detailed STM images of the clean surface allowed for the elimination of many of the possible (4×2) structures. In addition, the chemical makeup of the row atoms was determined by depositing Cl_2 onto the surface and observing the Cl chemisorption sites. Density functional theory (DFT) calculations were also performed to confirm the experimental findings. The most probable InAs(001)-c(8×2)/(4×2) reconstruction was identified as the undimerized β3(4×2) structure.

3.3 Experimental and Computational Techniques

Experiments were performed in two UHV chamber that were both equipped with low energy electron diffractometer (LEED), Auger electron spectrometer (AES), and different types of STMs. The majority of the STM experiments were performed on a Park Scientific VP STM. An Omicron LT STM was also employed for some of the experiments; images taken with the Omicron system are labeled within the text of the paper. As capped InAs(001) wafers were thermally decapped to the InAs(001)-c(8×2)/(4×2) surface by performing ramping cycles to ~450ºC. Details of the decapping procedure are discussed elsewhere.[68] LEED was used to verify the surface periodicity, after which the samples were transferred into the STM for analysis. This included obtaining atomically resolved filled and empty state STM images.

After the clean surface had been confirmed, Cl_2 was deposited onto the surface. This was achieved by opening a leak valve on the chamber and allowing 2% Cl_2 in N_2 to flow into the chamber until the pressure in the chamber reached 1×10^{-8} Torr. STM movies were made by continually taking STM images during the 30 min Cl deposition, which allowed for the monitoring of reacted Cl sites.

DFT calculations were used to confirm the experimental results. Plane wave (periodic boundary) calculations were performed using the Vienna *Ab-initio* simulation package (VASP) code.[51-54] For the current study, a nine atomic layer slab was used which was terminated by H atoms having a charge of 1.25 e⁻. In order to preserve the bulk like properties of the system, the bottom three layers of the slab, along with the H atoms, were frozen in bulk position. In addition, thirteen layers of vacuum were used to keep interactions with the top and bottom of the slabs to a minimum. Calculations were performed using the Perdew-Burke-Ernzerhof (PBE)[55] variant of the general gradient approximation. Atoms were modeled using projector augmented wave (PAW)[56,57] potentials as supplied by VASP. A 2×4×1 Monkhorst-Pack k-point sampling scheme was employed which resulted in the generation of 4 irreducible k-points in the first Brillouin zone. The plane wave cut off energy was set to 500 eV. The relaxation criteria were set to terminate the calculations once the forces were below 0.01 eV/Å. However, this level of accuracy was never reached. The forces dropped until the highest force was 0.06 eV/Å and subsequently the forces stabilized. It is possible that the inability of the slab to fully relax stems from the large overlap between the conduction and valence bands preventing the true ground state from being reached.

3.4 Experimental Results and Discussion

A.   Clean InAs(001)-*c*(8×2)/(4×2) surface

A large scale (450 × 450 Å^2) STM image of the clean surface is seen in Fig. 2(a). The image reveals bright long straight rows that run in the [110] direction. The rows are separated by ~17 Å and have a row thickness of ~7 Å. The effects of sample bias on the STM images were explored by taking filled [Fig. 2(b)] and empty [Fig. 2(c)] state images, in the same region. The bias dependent images show, that the trough structure is more readily resolved in empty state images, than in filled state images. These STM results are consistent with images published in literature.[77,78]

The information gleaned from the STM images can help eliminate some of the possible (4×2) structures. First, the row thickness can help determine how many dimers reside in the row. If the rows were made up of double dimers, then the row thickness should be comparable to the row thickness of the β2(2×4) reconstruction which has a two dimer row structure. The β2(2×4) reconstruction has rows that are ~9 Å thick: since the experimentally observed rows on the (4×2) structure are only ~7 Å wide this suggest that the (4×2) structure has a single dimer structure. This eliminates α(4×2), β(4×2), β2(4×2), and the ζ(4×2) reconstructions as possible structures for InAs(001)-*c*(8×2)/(4×2). Second, the rows in the STM images are straight and do not zigzag.   Therefore, the reconstruction cannot have multiple structures of

approximately the same energy. For example, Fig. 3(a) and 3(b) show energetically degenerate structures for the α2(4×2) reconstruction. Since the two structures are energetically degenerate, the experimental surface would contain a distribution of the two sites, Fig. 3(c). This would cause the rows in STM images to appear to zigzag. Since this is not observed in the InAs(001)-*c*(8×2)/(4×2) STM images, reconstructions α(4×2), α2(4×2), and α3(4×2) can be eliminated as possible structures. Lastly it has been well documented that the trough region of InAs(001)-*c*(8×2)/(4×2) is better resolved in empty state imaging.[77] This suggests that the dimers in the trough are made up of In dimers. This eliminates α(4×2), α3(4×2), β(4×2), and ζ(4×2) as possible reconstruction candidates.

From the STM images, all but two of the structures can be eliminated as the possible InAs(001)-(4×2) structure. The two remaining structures are the β3(4×2) and S(4×2) reconstructions. These structures differ in one important way; the S(4×2) reconstruction has As dimers on the row while the β3(4×2) reconstruction has In dimers on the row. Although the β3(4×2) and S(4×2) reconstructions have different row structures their trough structures are identical; both trough structures are comprised of two parallel In dimers.

B.   Defects on the InAs(001)-*c*(8×2)/(4×2) surface

For clean semiconductor surfaces, defect sites usually consist of missing atoms as opposed to contaminants, therefore, they can be used to verify structural models. If

a commonly found defect cannot be explained using the given structural model the structural model is most likely flawed. Figure 4(a) and 4(b) show filled and empty state images of the InAs(001)-$c(8\times2)/(4\times2)$ surface respectively; red circles have been drawn around six of the same type of trough defect sites. This type of defect site changes dramatically depending on the applied sample voltage. In filled state images, the defect appears as two bright spots that are separated by ~12.5 Å. In empty state images, the defect site images as a depression and causes the trough rungs to be separated by ~12.5 Å instead of ~8.5 Å. Kendrick *et al.* also observed the trough defect site on InAs(001)-$c(8\times2)/(4\times2)$ but they never identified the cause of the defect.[77]

The defect site is most likely two missing trough In atoms, which results in the trough structure shifting its reconstruction by one half of a unit cell, (Fig. 5). When the trough shifts by a half of unit cell, it causes the surface to shift between the (4×2) and the $c(8\times2)$ reconstructions. In order to determine if this is the correct defect site, it is helpful to imagine how this site should appear in both filled and empty state images. The missing In atoms, leave two As atoms that are only bonded to two In atoms. Therefore, these As atoms should both have two filled or partially filled dangling bonds. Although it is unclear exactly how this charge redistributes, if some of the charge was relocated into the dangling bonds of the nearby In atoms it would cause these atoms to image slightly brighter in filled state images. In empty state images this defect would be expected to shift the trough rung spacing from ~8.5 Å to ~12.5 Å.

Since the defect sites can be explained within the β3(4×2) and S(4×2) models, each of these is a viable contender for the InAs(001)-c(8×2)/(4×2) reconstruction.

C.   Atomically resolved row structure

Both the β3 and the S models have the same trough structure, therefore, the trough defect site did not allow for the elimination of either of these two structures. In an effort to identify the row structure, atomic resolved images of the row were taken with an Omicron LT STM. Figure 6 shows an STM image of the InAs(001)-c(8×2)/(4×2) surface along with a line scan down the length of a row. The line scan reveals that the row is comprised of individual atoms that are separated by ~4.3 Å.

The atomically resolved STM image along with the line scan reveals that the S(4×2) model cannot be the correct reconstruction for InAs(001)-c(8×2)/(4×2). The S(4×2) model has dimers that run perpendicular to the row which would be expected to image wider in the [$\bar{1}$10] than the [110] which is in conflict with the experiments. In addition, if the S(4×2) model was correct, one would expect a commonly seen defect site to be a missing surface As atom. This would cause the row to narrow whenever a defect site was present. However, this has never been seen experimentally.

The atomically resolved image and line scan also reveal problems with the β3(4×2) model. The β3(4×2) model has dimers that run in [110] direction. These dimers should be separated by ~8.5 Å. The line scan reveals however, that along the

row the spacing is ~4.3 Å. This suggests that instead of having dimers on the row, the rows are comprised of undimerized atoms. Figure 7 shows a ball-and-stick diagram of the undimerized $\beta3(4\times2)$ structure (also referred to as the $\beta3(4\times2)'$ reconstruction).

D.   Cl adsorbed onto InAs(001)-*c*(8×2)/(4×2)

Identifying the row atoms as In or As atoms can help further confirm the (4×2) reconstruction. However, atomic composition is difficult to identify in STM images; in order to identify the atomic composition of the surface, other techniques need to be employed. Cl has been shown to preferentially react with III atom in III-V semiconductors.[79,80] This is impart due to the fact that Cl is extremely electronegative and is inclined to bond to atoms which are good electron donors.

STM images of the clean InAs(001)-*c*(8×2)/(4×2) surface and the same area of the surface after Cl_2 deposition are seen in Fig. 8(a) and 8(b) respectively. After Cl_2 deposition, the STM image reveals depressions on the rows. These depressions are the reacted Cl sites. AES was used to further confirm that Cl was deposited on the surface. Since the Cl atoms adsorbed onto the rows, it is reasonable to assume that the rows are comprised of In atoms on InAs(001)-*c*(8×2)/(4×2). As previously mentioned, it is believed that the trough is also comprised of In dimers. However, no reacted sites were ever observed in the trough region. This is most likely due to poor tip resolution. These findings further suggest that the $\beta3(4\times2)'$ structure is the most likely reconstruction for InAs(001)-*c*(8×2)/(4×2).

3.5 Computational Results and Discussion

The experimental results strongly suggest that the InAs(001)-c(8×2)/(4×2) reconstruction is the β3(4×2)' structure. In order to further confirm these findings, DFT was used to simulate both the β3(4×2) and the β3(4×2)' reconstructions. Top-down views of the two slabs are seen in Fig. 9. Each compositional slab consists of two unit cells.

Tersoff and Hamann STM simulations were calculated in order to compare the DFT results with the experimental findings.[65] Filled and empty state STM simulations of the β3(4×2) and the β3(4×2)' along with experimental images are presented in Fig. 10(a) and 10(b). Filled state STM simulations of both reconstructions show that the prominent features are caused by electrons tunneling out of the filled dangling bonds of the second layer As atoms. Subtle differences exist between the filled state images of the two structures. In the β3(4×2) STM simulation, In dimers are position in the center of four As atoms. These In dimers cause a slight rise in electron density with ~8.5 Å periodicity. This rise in electron density has never been seen experimentally. The row In atoms of the β3(4×2)' reconstruction are aligned with the As atoms in the $[\bar{1}10]$ direction, eliminating the increases in electron density that are calculated for the β3(4×2) structure. In empty state STM simulations, the majority of the electron density is a result of electrons tunneling into the empty dangling bonds of the surface

In atoms. The β3(4×2) structure has In dimers and the β3(4×2)' structure has undimerized In atoms, therefore, the spacing in row charge maximums are calculated to be ~8.5 Å for β3(4×2) and ~4.3 Å for β3(4×2)'. Experimentally only charge maximums with ~4.3 Å periodicity have been observed. Therefore, the β3(4×2)' STM simulations are a closer fit to experimental findings.

The experimental data suggests that the InAs(001)-c(8×2)/(4×2) reconstruction is the β3(4×2)' structure. This structure is unusual because it contains undimerized surface atoms. In order to deduce why it is preferable to have undimerized row In atoms, the bonding geometries within both the β3(4×2) and β3(4×2)' structures have been studied.

If the surface atoms are dimerized then the In atoms in the dimer should be sp^2 hybridized, which should have As-In-As ideal bond angles of 120º [Fig 11(a)]. However, the DFT computation shows this bond angle is ~142º consistent with a large amount of strain on the rows. In addition, the As atoms directly bonded to these In dimers have a partially filled dangling bond. To calculate the number of electrons in the dangling bond, it is assumed that atoms on the surface give the same number of electrons to bonds that they do in the bulk (similar to the electron counting model). Therefore, when an As atom bonds to an In atom, the As atom contributes 5/4 of an electron to the bond. If this assumption is employed, dangling bonds on the surface As atoms contain 5/4 e⁻. It is energetically unfavorable to have a radical on the surface thereby making the reconstruction less favorable.

If the surface In atoms are undimerized, then the first layer In atoms should be sp hybridized. DFT computations show the As-In-As bond angle is 179º which is essentially the ideal sp hybridized bond angles [Fig. 11(b)]. The distribution of surface electrons also changes significantly for the β3(4×2)' reconstruction. Having undimerized In atoms allows the In atoms to form double bonds to the surface As atoms. Electrons that were in the partially filled dangling bonds on the surface As atoms in the β3(4×2) structure, relocate to form the double bond thereby making the system more energetically favorable.

A closer look can be taken at bond length to confirm that first layer In atoms are sp^2 hybridized in the β3(4×2) reconstruction and sp hybridized in the β3(4×2)' reconstruction. The first layer In atoms in the β3(4×2) reconstruction should form single bonds to the second layer As atoms, conversely, the first layers In atoms should form double bonds with the second layer As atoms for the β3(4×2)' reconstruction. Double bonds are shorter than single bonds, therefore, comparing the dimerized and undimerized bond lengths can confirm the hybridization of the first layer In atoms. The As-In bond length in the β3(4×2) structure is 2.64 Å while the As-In bond length in the β3(4×2)' structure is 2.52 Å showing that a double bond has most likely formed for the β3(4×2)' reconstruction while a single bond has formed for the β3(4×2) reconstruction.

Although only the β3(4×2)' reconstruction is observed experimentally, this geometry is degenerate with the β3(4×2) structure (0.04 eV energy difference between the two structures). This difference in energy is very small considering it is spread out

between the 12 row In atoms and the As atoms to which they are bonded. In addition, the 0.04 eV difference might have a significant error. DFT has been well documented to do a poor job of calculating electronic structures of narrow band gap semiconductors such as InAs. The electronic structure of the InAs slabs show a significant overlap between the conduction band and the valence band. This overlap most likely causes deviations between the calculated ground state and the actual ground state of the system. This suggests that the atomic placements are slightly askew, leading to higher than normal errors in the energy. These errors may be significant enough to widen the energy gap between the two structures.

3.6 Conclusion

Filled and empty state STM images helped identify the InAs(001)-c(8×2)/(4×2) reconstruction as the β3(4×2)' structure. This reconstruction was found to significantly different from other surfaces because the row In atoms formed double bonds. These double bonds were able to form due to In's ability to be sp hybridized. DFT STM simulations were also found to be in good agreement with the β3(4×2)' model.
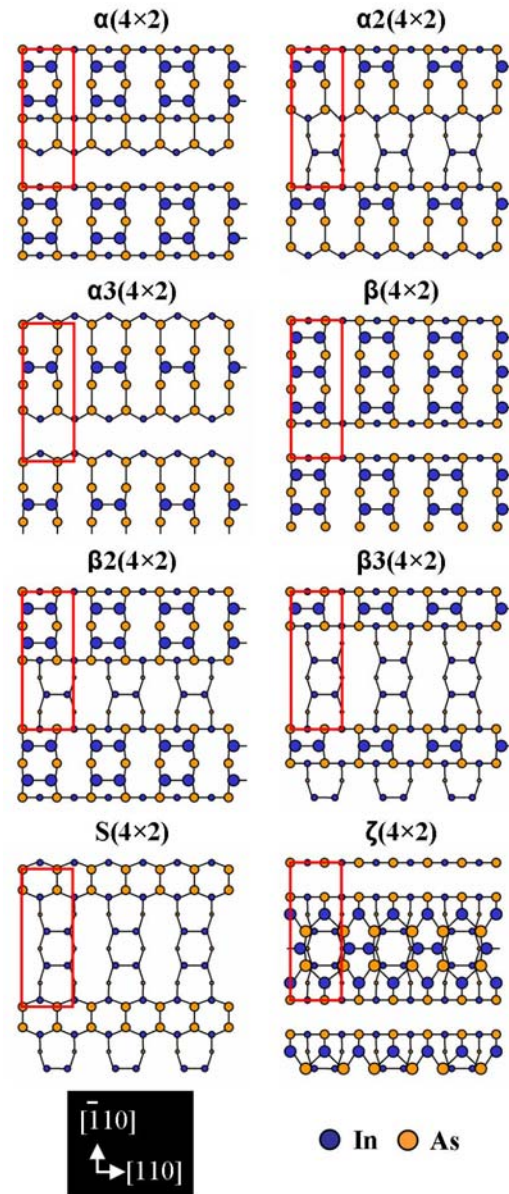
3.7 Figures

FIGURE 3.1 Possible structures for the InAs(001)-(4×2) reconstruction. The red boxes denote the unit cells of the systems.
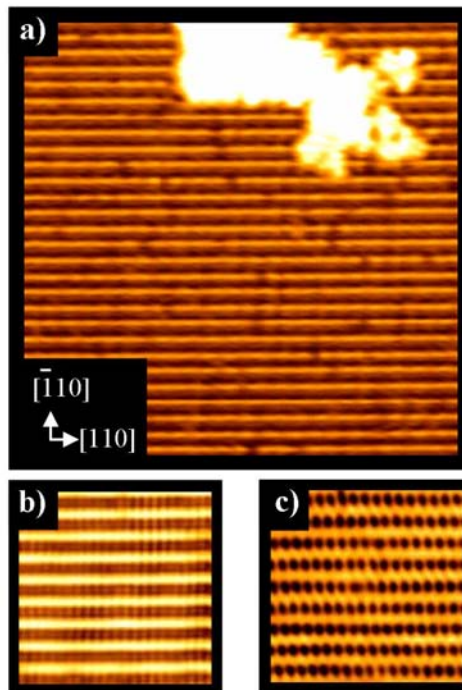
FIGURE 3.2 (a) 450×450 Å^2 STM image (V_s = -2 V, I_t = 0.5 nA) of the InAs(001)-$c(8\times2)/(4\times2)$ surface. (b) 150×150 Å^2 filled state image (V_s = -2 V, I_t = 0.2 nA) of the InAs(001)-$c(8\times2)/(4\times2)$ surface reconstruction (c) 150×150 Å^2 empty state image (V_s = 2 V, I_t = 0.2 nA) of the same area of InAs(001)-$c(8\times2)/(4\times2)$.
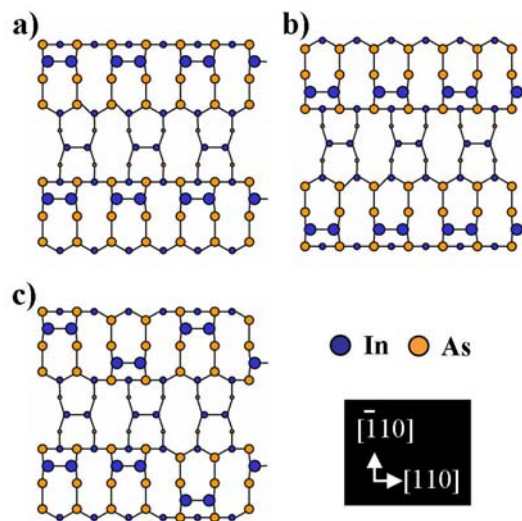
FIGURE 3.3 (a) Ball-and-stick diagram of the α2(4×2) reconstruction. (b) Ball-and-stick diagram of an energetically degenerate structure of the α2(4×2) reconstruction. (c) Ball-and-stick diagram of what an experimental α2(4×2) surface would look like.

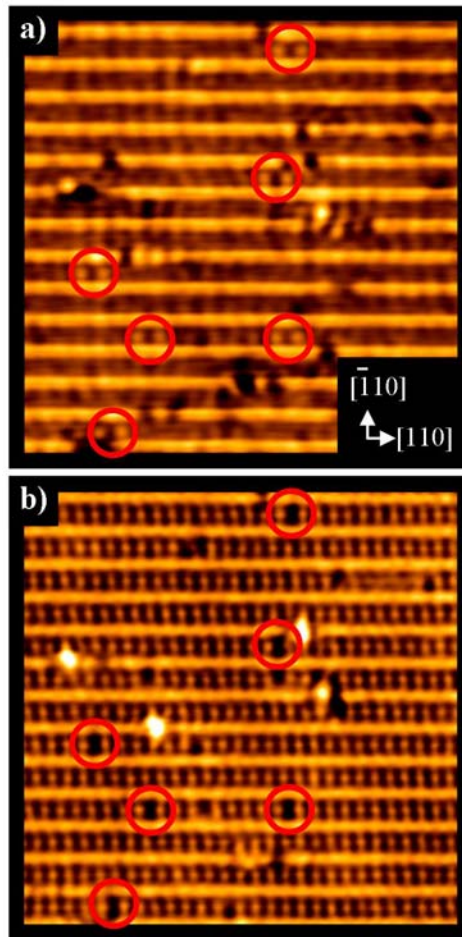FIGURE 3.4 (a) 225 × 225 Å^2 filled state STM image (V_s = -2 V, I_t = 0.2 nA) of the InAs(001)-c(8×2)/(4×2) surface with most common row defect circled in red. (b) 225 × 225 Å^2 empty state STM image of the same area (V_s = 2 V, I_t = 0.2 nA) of the InAs(001)-c(8×2)/(4×2) surface with same defects circled in red.
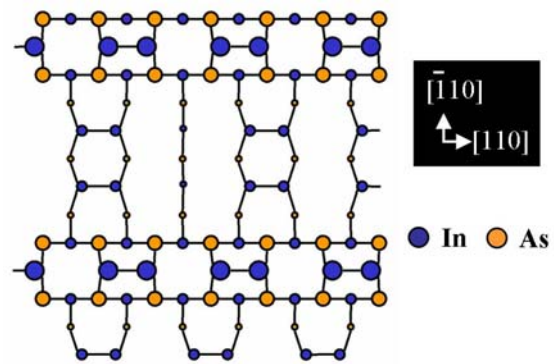
FIGURE 3.5 Ball-and-stick diagram of the proposed defect site on InAs(001)-β3(4×2).

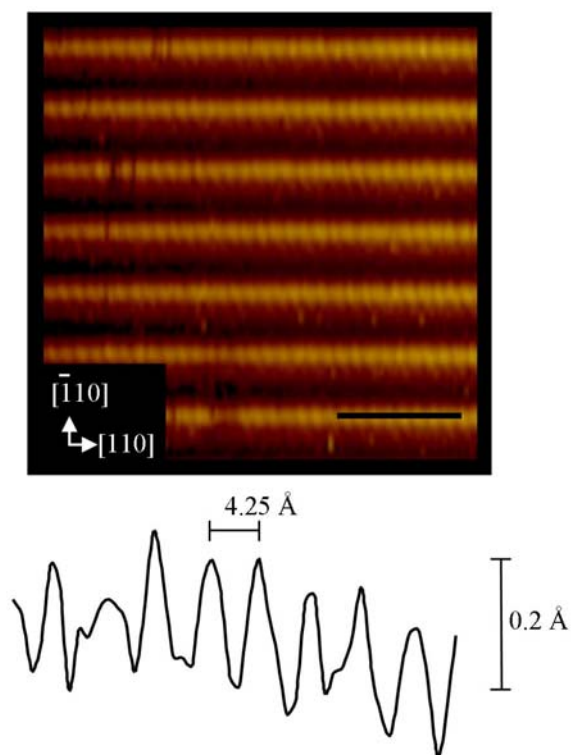FIGURE 3.6 120 × 120 Å^2 atomically resolved STM image (V_s = -2.2 V, I_t = 0.05 nA) and line scan corresponding to the black line on the STM image showing individual atoms separated by ~4.3 Å.
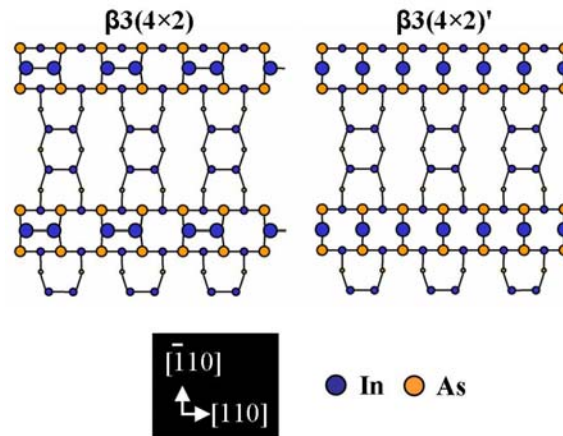
FIGURE 3.7 Ball-and-stick diagrams of the β3(4×2) and the β3(4×2)' reconstructions.
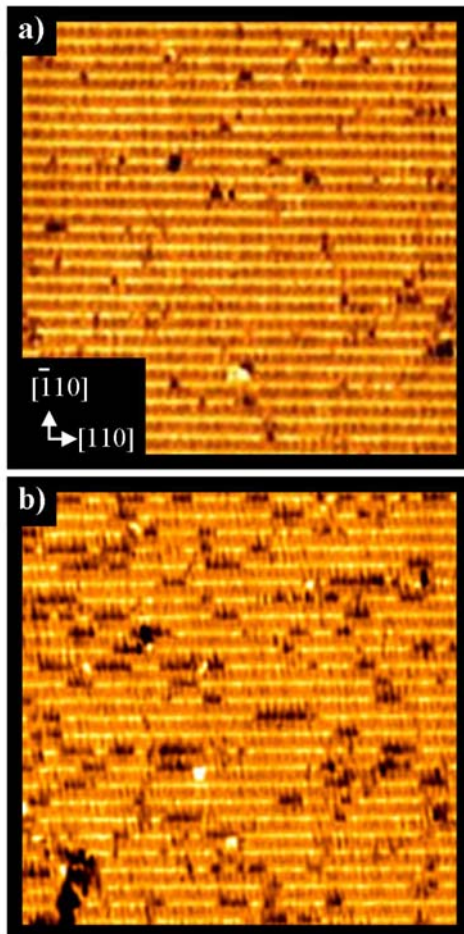
FIGURE 3.8 (a) 425 × 425 Å^2 STM image (V_s = -1 V, I_t = 0.2 nA) of the clean InAs(001)-c(8×2)/(4×2) surface. (b) 425 × 425 Å2 STM image (V_s = -1 V, I_t = 0.2 nA) of the same location after 30 min deposition of Cl_2.
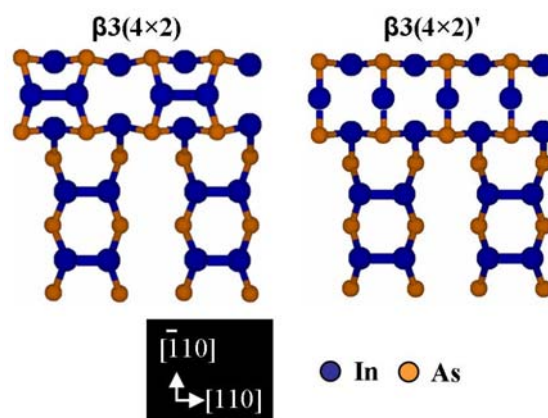
FIGURE 3.9 Top-down views of the β3(4×2) and β3(4×2)' computational slabs.

β3(4×2) / β3(4×2)'
Experimental

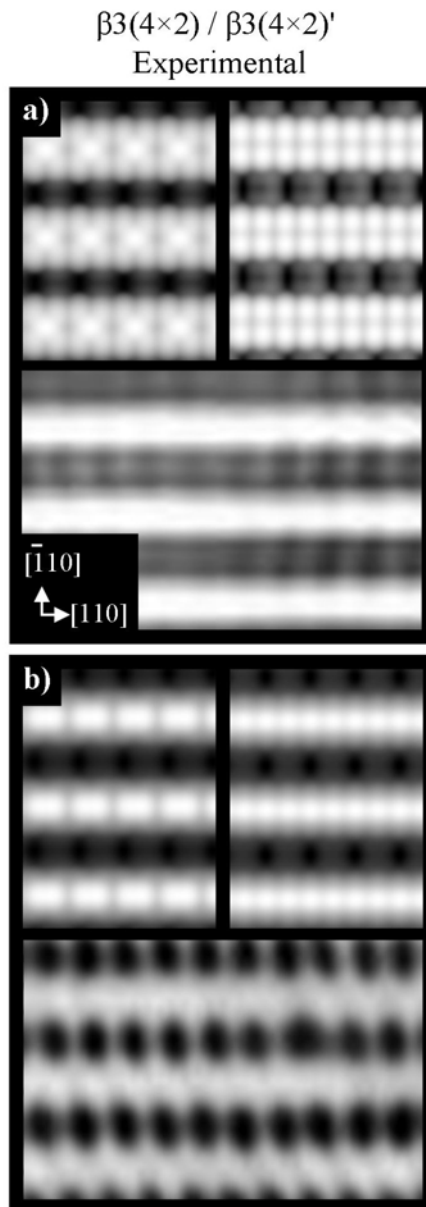FIGURE 3.10 (a) Filled state STM simulations of the β3(4×2) (top left) and the β3(4×2)' (top right) reconstructions along with a filled state STM image (V_s = -2 V) (bottom). (b) Empty state STM simulation of the β3(4×2) (top left) and the β3(4×2)' (top right) reconstructions along with a empty state STM image (V_s = 2 V) (bottom).

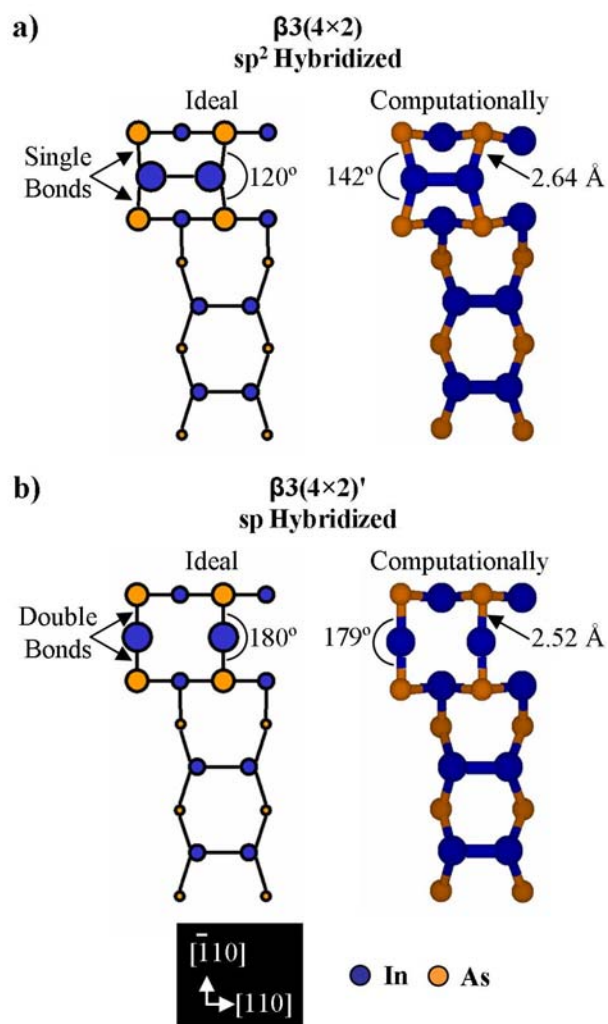FIGURE 3.11 Ideal and computational bonding angles for the (a) β3(4×2) and (b) β3(4×2)' reconstructions along with In-As bond lengths.

3.8 Acknowledgments

This Chapter is being prepared for publication:

CHAPTER FOUR

Electronic Properties of Adsorbates on In$_{0.37}$Ga$_{0.63}$As(001)-(2×4)

4.1 Abstract

The molecular and electronic structures of In$_2$O and Ga$_2$O bonding to the As-rich In$_{0.37}$Ga$_{0.63}$As(001)-(2×4) surface were investigated using density functional theory (DFT) calculations. The DFT calculations revealed that the bonding enthalpies of In$_2$O and Ga$_2$O on In$_{0.37}$Ga$_{0.63}$As(001)-(2×4) were almost identical to the bonding enthalpies of Ga$_2$O and In$_2$O on GaAs(001)-(2×4). Although the density of states (DOS) calculations for oxides bonding onto In$_{0.37}$Ga$_{0.63}$As(001)-(2×4) and GaAs(001)-(2×4) are very similar, subtle differences are observed. In both cases the Fermi level pinning became more severe as the number of molecules in close proximity was increased. However, it took more oxide molecules bonded in close proximity before Fermi level pinning was seen for InGaAs than for GaAs. The alloy structure had only minor effects on the bonding geometry and the electronic structure of the adsorbates. Instead, the lower density of band edge states for oxides bonding on the In$_{0.37}$Ga$_{0.63}$As(001)-(2×4) *vs.* GaAs(001)-(2×4) is due to band gap size differences.

4.2 Introduction

InGaAs is a promising material for long wavelength optical communication devices.[81] Several groups have attempted to construct an InGaAs metal oxide semiconductor field effect transistor (MOSFET) device.[1,2] Currently, the InGaAs devices have substrates that are either GaAs or InP. Increasing the In content raises the mobility of the alloy, but lattice matched alloys are limited to ~30% In content for very thin layers of InGaAs (~100 Å) on GaAs. While higher In content alloys can be grown on InP, InGaAs/GaAs is of technical interest due to the availability of large GaAs substrates and the ability to grow GaAs on Ge or GOI (Ge on insulator) wafers. Multiple studies have investigated oxides deposited on InGaAs in order to ascertain which oxide induces the least amount of states in the band gap region. These oxides include $Ga_2O_3(Gd_2O_3)$, Al_2O_3, and the thermal oxidation of AlAs.[1,2,81] Although groups have been able to demonstrate both working depletion[2] and enhancement mode[1] MOSFET devices, the electronic properties of these devices could be improved with an atomic understanding of the oxide/InGaAs interface.

In spite of the technological importance of InGaAs(001), only recently has work been performed to understand and characterize the surface at the atomic level. In order to characterize the clean surface, several groups have performed scanning tunneling microscopy (STM) studies to identify the different surface reconstructions of InGaAs(001). Although there are still disagreements about the exact surface

reconstructions, most groups agree that there are at least (2×4) and (n×3) surface reconstructions.[82-84]

Very few computational papers have been published on InGaAs(001),[85-90] and no papers address oxide bonding on the InGaAs(001)-(2×4) surface. In this manuscript, DFT calculations will be presented of the clean $In_{0.37}Ga_{0.64}As(001)$-(2×4) surface along with calculations predicting the bonding geometries of In_2O and Ga_2O bonding with the clean surface. The 37% In content was chosen because it is close to the maximum In content for very thin InGaAs layers on GaAs.

4.3 Computational Techniques

$In_{0.37}Ga_{0.63}As(001)$-(2×4) was modeled using plane-wave (periodic boundary) DFT calculations. The calculations were performed using the Vienna *ab initio* simulation package (VASP).[51-54] Slabs consisted of eight atomic layers with the bottom layer being terminated with H atoms. In order to preserve the bulk like properties of the system, the bottom three layers of the slab, along with the H atoms, were frozen in bulk position. Eleven layers of vacuum were used to avoid interactions between the top and the bottom of the slabs. The calculations were performed using the PW91 variant of the general gradient approximation.[55] Atoms were modeled using ultrasoft pseudopotentials as supplied by VASP.[69,91] A 4×2×1 Monkhorst-Pack[58] k-point sampling scheme was employed which resulted in the generation of four

irreducible k-points in the first Brillouin zone. The plane wave cut off energy was set to 475 eV, and the slab was considered fully relaxed when the forces were less than 0.03 eV/Å. The error in these calculations is assumed to be ±0.1 eV. A detailed discussion of how the ±0.1eV error was reached is presented elsewhere.[68]

4.4 Results and Discussion

A. Clean In$_{0.37}$Ga$_{0.63}$As(001)-(2×4) surface

DFT calculations have been performed on numerous III-V semiconductors. However, when modeling a compound III-V semiconductor, such as InGaAs, the procedure is slightly more complicated due to variability in the locations of the In and Ga atoms. Figure 1(a) shows a ball and stick diagram of the clean InGaAs(001)-(2×4) surface. As atoms are depicted as orange circles and In or Ga atoms are depicted as black circles. An In concentration of 37% was used for this study resulting in a slab that contained 11 In atoms and 19 Ga atoms.

The main complication in deciding the placement of the In and Ga atoms is that although the placements can be random within the slab, once the slab is tiled in all directions, there is long-range order. In an effort to verify that long-range order will not effect the calculations, four different slabs were constructed with random placements of the Ga and In atoms [Fig. 1(b)-1(e)]. The four slabs had energies of -280.23, -280.06, -280.75, and -289.48 eV. The span in energies results from

differences in surface energy of the structures along with bulk energy differences most likely due to strain. The molecular beam epitaxially grown samples are expected to have a random placement of In and Ga atoms in the bulk with slightly higher In concentrations at the surface.[92]

Although the differences in total energy between the four slabs are not substantial, it is also important to verify that the In and Ga placements do not effect the electronic properties of the system. Figure 2 shows the density of states (DOS) of the four different geometries. From the plot, it can be seen that the electronic properties of the slabs remain the same regardless of the placements of the In or the Ga atoms. Therefore, only one bonding geometry was chosen [Fig. 1(b)] for subsequent calculations upon the bonding of In_2O and Ga_2O molecules to the $In_{0.37}Ga_{0.63}As(001)$-(2×4) surface.

B. In_2O and Ga_2O bonding to $In_{0.37}Ga_{0.63}As(001)$-(2×4)

The In_2O and Ga_2O bonding sites along with the enthalpies of adsorption are presented in Fig. 3. Winn *et al.*[93] did a similar study of In_2O and Ga_2O bonding to the GaAs(001)-(2×4) surface; a summary of their findings along with the findings in the current paper are seen in Table 1. Although the computational methods vary slightly, the overall trends between the two systems can be compared.

Calculations were performed on three different bonding sites for both In_2O and Ga_2O. The row bonding site forms when an oxide molecule inserts into the As row

dimers; this is referred to as a "row insertion" site. In addition to the row site, two different trough sites were also examined. The first trough site is the "trough over dimer" site and forms when an oxide molecule bonds to the group III atom at the trough edge making a bridge site over an As trough dimer. The second trough site is a "trough between dimer" site and forms when an oxide molecule bonds to the group III molecule at the trough edge making a bridge site between the As trough dimers.

The enthalpies of adsorption for the In_2O bonding sites on $In_{0.37}Ga_{0.63}As(001)$-$(2\times4)$ are presented in Fig. 3(a). The row insertion site and the trough over dimer site are essentially degenerate in energy. Therefore, it is reasonable to assume that In_2O molecules will occupy both the row insertion sites and the trough over dimer sites, even at low coverage.

For $In_2O/In_{0.37}Ga_{0.63}As(001)$-$(2\times4)$, the significant difference in adsorption energies between the two trough sites is most likely a result of dissimilar bonding environments. An In_2O molecule that bonds between the trough As dimers has an unfavorable interaction with the filled dangling bonds on the trough As dimers while the oxide molecule that bonds over the trough As dimer has no unfavorable interactions with the filled dangling bonds on the trough As dimers. This results in the trough between dimer site being less energetically favorable than the trough over dimer site.

Figure 3(b) gives the enthalpies of adsorption for the Ga_2O bonding sites on $In_{0.37}Ga_{0.63}As(001)$-$(2\times4)$. Although one might expect Ga_2O and In_2O adsorption energies to be nearly the same, they have major differences. The Ga_2O row insertion

site is significantly more stable than the In_2O row insertion site (-1.86 eV/Ga_2O and -1.12 eV/In_2O, respectively). Resulting in the Ga_2O row insertion site being significantly more stable than any of the other Ga_2O bonding geometers on $In_{0.37}Ga_{0.63}As(001)$-(2×4). Therefore, at low coverage only the Ga_2O row insertion sites are expected to form on $In_{0.37}Ga_{0.63}As(001)$-(2×4). The difference in Ga_2O and In_2O stability on GaAs(001)-(2×4) results from the stronger Ga-As bonds forming a more stable row insertion site than the weaker In-As.[93] Since the same type of bonds are formed when In_2O and Ga_2O bond to $In_{0.37}Ga_{0.63}As(001)$-(2×4), the energy difference for the row insertion sites on $In_{0.37}Ga_{0.63}As(001)$-(2×4) can again be ascribed to the Ga-As and In-As bond strength differences.

The Ga_2O/$In_{0.37}Ga_{0.63}As(001)$-(2×4) enthalpies of adsorption clearly show that the most favorable bonding geometry is the row insertion site. The differences in adsorption energies between the Ga_2O/$In_{0.37}Ga_{0.63}As(001)$-(2×4) bonding geometries are attributed to three causes. First, Ga-As bonds are stronger than Ga-Ga bonds, causing the row site to be more stable than the trough sites.[93] Second, the row site forms four new bonds while the trough sites only form two, which causes the row site to be more stable than the trough sites. Third, as with In_2O bonding to $In_{0.37}Ga_{0.63}As(001)$-(2×4), unfavorable interaction exists between the filled dangling bonds on the trough As dimer and the trough between dimer site.

Although no experiments have been performed to verify the In_2O or the Ga_2O bonding sites on $In_{0.37}Ga_{0.63}As(001)$-$c$(2×8)/(2×4), the computations can be compared to the experimentally found binding sites for In_2O and Ga_2O on GaAs(001)-

$c(2\times8)/(2\times4)$. Experimental results reveal that In_2O bonds to both the row and the trough regions on GaAs(001)-$c(2\times8)/(2\times4)$ at low coverage. Conversely, experiments show that Ga_2O only bonds to the row on GaAs(001)-$c(2\times8)/(2\times4)$ at low coverage. These results are consistent with the computational findings for In_2O and Ga_2O on $In_{0.37}Ga_{0.63}As(001)$-$(2\times4)$.

C.   Density of states and projected density of states calculations

Previous DOS calculations for In_2O and Ga_2O on GaAs(001)-(2×4) were performed on a double slab (two unit cells put together).[93] This allowed for both half coverage of sites (every other site filled in) and full coverage of sites (every site filled in). In the current study, only one unit cell was simulated, therefore, only full coverage results were obtained. Previous studies found that none of the half coverage sites on GaAs(001)-(2×4) pinned the Fermi level.[93] However, as the coverage increased, states began to form in the band gap region for both In_2O and Ga_2O bonded to GaAs(001)-(2×4). However, none of the high coverage calculated sites were ever seen experimentally for Ga_2O on GaAs(001)-(2×4).

Figure 4(a) shows the DOS for the three different In_2O bonding sites. Of the three sites, only one site introduces states into the band gap (row insertion site). As the concentration of In_2O molecules in close proximity to each other increases to complete trough coverage (every possible trough site filled in which utilizes both

types of trough sites), the density of states induced in the band gap region also increases [Fig. 4(b)].

The DOS results for In_2O on $In_{0.37}Ga_{0.63}As(001)$-$(2\times4)$ can be compared to the DOS results for In_2O on $GaAs(001)$-(2×4). For In_2O on $GaAs(001)$-(2×4), the full coverage insertion and full coverage over dimer sites both had states within the band gap region with the largest density of states in the bang gap region being generated by the full coverage row insertion site.[93] Conversely, when In_2O bonds onto $In_{0.37}Ga_{0.63}As(001)$-$(2\times4)$, the only site that generates states in the band gap region is the row insertion site. These calculations suggest that Fermi level pinning is less severe for In_2O bonding to $In_{0.37}Ga_{0.63}As(001)$-$(2\times4)$ than for In_2O bonding to $GaAs(001)$-(2×4). When In_2O bonds to either $In_{0.37}Ga_{0.63}As(001)$-$(2\times4)$ or $GaAs(001)$-(2×4), it induces states near the band edges. Since InGaAs has a smaller band gap than GaAs, these In_2O induced states most likely reside outside the band gap region for InGaAs while they reside inside the band gap region for GaAs. As the In_2O coverage increases the number of states also increases causing the states to be observed in the band gap region for InGaAs.

Figure 5(a) shows the DOS for the three different Ga_2O bonding geometries on $In_{0.37}Ga_{0.63}As(001)$-$(2\times4)$. The only site that causes state formation in the band gap region is the trough between dimer site. The calculated Ga_2O/ $In_{0.37}Ga_{0.63}As(001)$-$(2\times4)$ sites are comparable to full coverage sites for $Ga_2O/GaAs(001)$-(2×4) which have pinned Fermi levels for both the row full coverage insertion and the trough full coverage over dimer sites.[93]

If the Ga_2O concentration is increased to complete trough coverage by bonding Ga_2O molecules in every available trough site (filling in all between and over dimer sites) on $In_{0.37}Ga_{0.63}As(001)$-$(2\times4)$, the Fermi level pinning worsens [Fig. 5(b)]. These results suggest that similar to GaAs the Fermi level pinning gets more severe as additional Ga_2O molecules bond in close proximity to each other.[93] However, for InGaAs a greater Ga_2O coverage is needed compared to GaAs before Fermi level pinning is observed. InGaAs has a smaller band gap than GaAs, therefore, some of the states that are seen when Ga_2O bonds with $GaAs(001)$-(2×4) are located outside the band gap region for InGaAs.

4.5 Conclusion

DFT calculations were performed to simulate In_2O and Ga_2O bonding to $In_{0.37}Ga_{0.63}As(001)$-$(2\times4)$. Although the adsorption energies are nearly the same for In_2O and Ga_2O adsorbing onto $In_{0.37}Ga_{0.63}As(001)$-$(2\times4)$ or $GaAs(001)$-(2×4), the electronic properties differ slightly. In both cases, increasing the density of oxide molecules increases the density of states in the band gap. However, the number of states in the band gap region was smaller for the oxides on $In_{0.37}Ga_{0.63}As(001)$-$(2\times4)$ than on $GaAs(001)$-(2×4). In_2O and Ga_2O induced states are mainly located at the band edges. The InGaAs band gap is smaller than the GaAs band gap causing a significant amount of the pinning states to be located outside the band gap region for

InGaAs. This suggests that in general, forming an unpinned oxide interface on narrow band gap semiconductors may be easier than on wide band gap semiconductors. It also suggests that the presence of disorder in the placement of atoms in ternary semiconductors has little effect on the atomic and electronic structure of the interface when the atoms are chemically similar (Ga and In as opposed to Ga and Al).

4.6 Figures

FIGURE 4.1 (a) Ball-and-stick diagram of the clean InGaAs(001)-(2×4) surface. (b) Side and top-down views of geometry 1. (c) Side and top-down views of geometry 2. (d) Side and top-down views of geometry 3. (e) Side and top-down views of geometry 4.

As

Ga or In

$[\bar{1}10]$
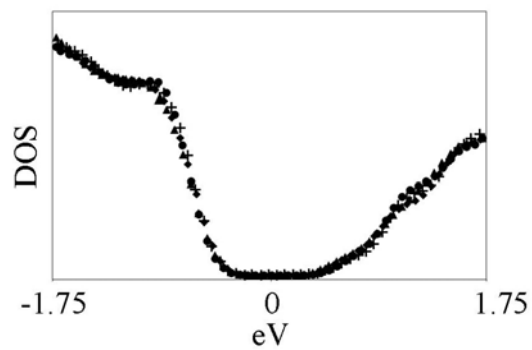
$[110]$

As   Ga   In   H
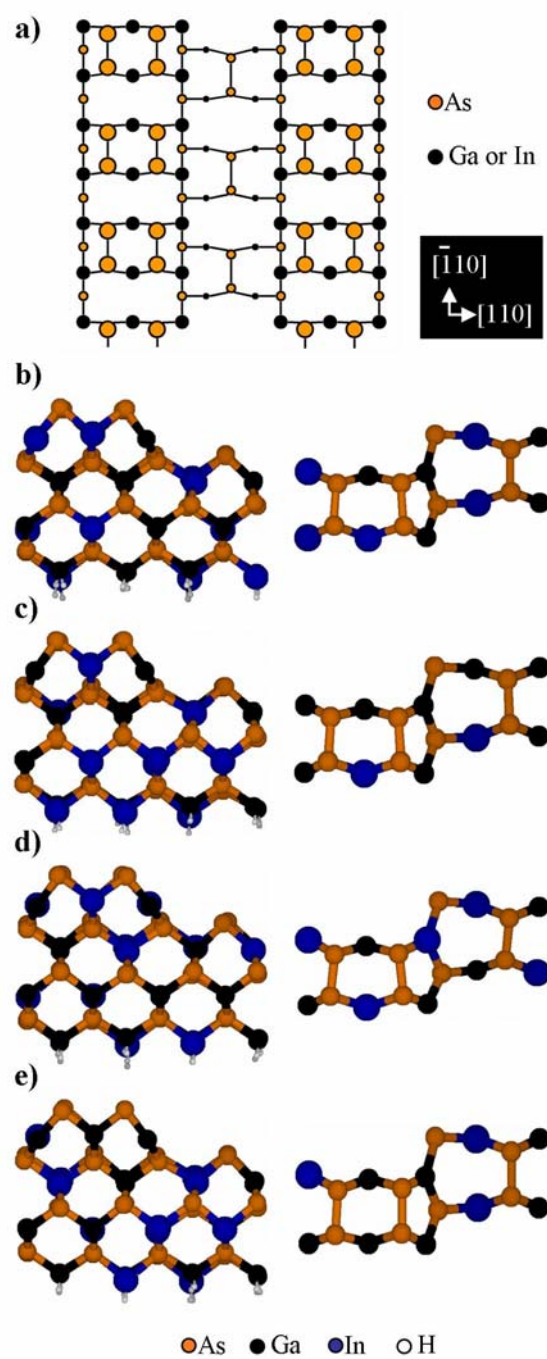
FIGURE 4.2 DOS of four different slabs with random In placements: geometry 1(●), geometry 2 (▲), geometry 3(+), and geometry 4(♦). All of the DOS line up, therefore, the In placement does not effect the electronic properties of the slab.
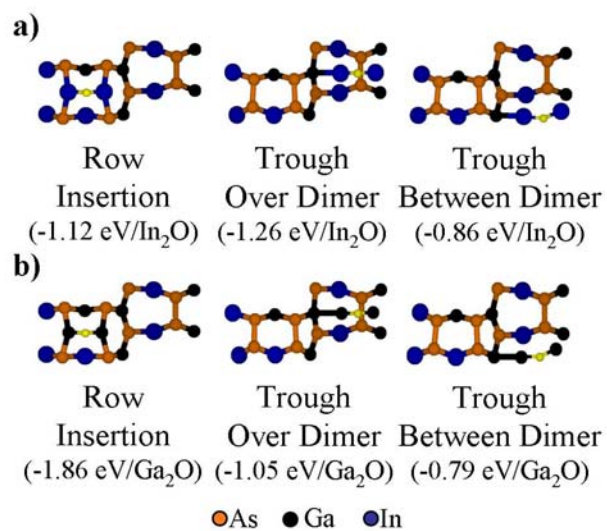
FIGURE 4.3 Top-down views of the (a) In_2O and (b) Ga_2O bonding sites on $In_{0.37}Ga_{0.63}As(001)$-$(2\times4)$.

FIGURE 4.4 (a) DOS of the single In_2O bonding sites on $In_{0.37}Ga_{0.63}As(001)$-$(2\times4)$: clean surface (black solid line), row insertion site (●), trough over dimer (▲), and trough between dimer (+) sites. (b) DOS of the clean surface (black solid line) and a surface with the trough completely filled in with In_2O molecules (every over and between dimer site occupied) (●).

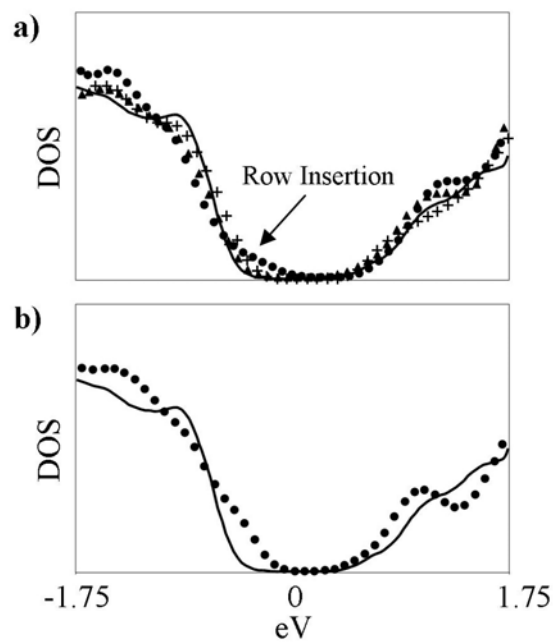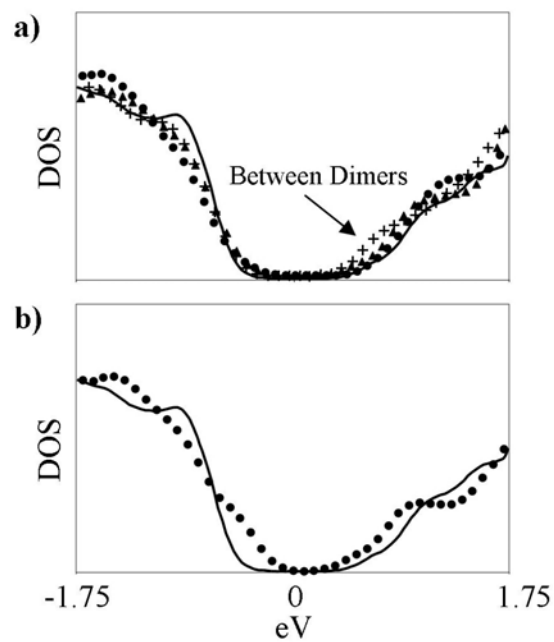FIGURE 4.5 (a) DOS of the single Ga$_2$O bonding sites on In$_{0.37}$Ga$_{0.63}$As(001)-(2×4): clean surface (black solid line), row insertion (●), trough over dimer (▲), and trough between dimer (+) sites. (b) DOS of the clean surface (black solid line) and a surface with the trough completely filled in with Ga$_2$O (every over and between dimer site occupied) (●).

4.7 Tables

TABLE 4.1 Summary of the findings for In_2O and Ga_2O bonding to the GaAs(001)-(2×4) and $In_{0.37}Ga_{0.63}As$(001)-(2×4).

	GaAs (ΔH_{abs})	$In_{0.37}Ga_{0.63}As$ (ΔH_{abs})
In_2O Half Coverage Insertion	-1.18 eV/In_2O	N/A
In_2O Full Coverage Insertion	-1.01 eV/In_2O	-1.12 eV/In_2O
In_2O Half Coverage Over Dimers	-1.26 eV/In_2O	N/A
In_2O Full Coverage Over Dimers	-1.24 eV/In_2O	-1.26 eV/In_2O
In_2O Half Coverage Between Dimers	-0.86 eV/In_2O	N/A
In_2O Full Coverage Between Dimers	Unknown	-0.86 eV/In_2O
Ga_2O Half Coverage Insertion	-1.87 eV/Ga_2O	N/A
Ga_2O Full Coverage Insertion	-1.79 eV/Ga_2O	-1.86 eV/Ga_2O
Ga_2O Half Coverage Over Dimers	-1.06 eV/Ga_2O	N/A
Ga_2O Full Coverage Over Dimers	-1.04 eV/Ga_2O	-1.05 eV/Ga_2O
Ga_2O Half Coverage Between Dimers	-0.69 eV/Ga_2O	N/A
Ga_2O Full Coverage Between Dimers	Unknown	-0.79 eV/Ga_2O

Grayed box denote pinned structures

4.8 Acknowledgments

This chapter is being prepared for publication:

The dissertation author was the primary author and researcher of this paper.

REFERENCES

1   F. Ren, J. M. Kuo, M. Hong, W. S. Hobson, J. R. Lothian, J. Lin, H. S. Tsai, J. P. Mannaerts, J. Kwo, S. N. G. Chu, Y. K. Chen, and A. Y. Cho, IEEE Electron Device Letters **19** (8), 309 (1998).

2   P. D. Ye, G. D. Wilk, B. Yang, J. Kwo, H. J. L. Gossmann, M. Hong, K. K. Ng, and J. Bude, Applied Physics Letters **84** (3), 434 (2004).

3   N. Yokoyama, T. Mimura, and M. Fukuta, IEEE Transactions on Electron Devices **27** (6), 1124 (1980).

4   J. Y. Wu, H. H. Wang, Y. H. Wang, and M. P. Houng, IEEE Transactions on Electron Devices **48** (4), 634 (2001).

5   Y. C. Wang, M. Hong, J. M. Kuo, J. P. Mannaerts, J. Kwo, H. S. Tsai, J. J. Krajewski, Y. K. Chen, and A. Y. Cho, IEEE Electron Device Letters **20** (9), 457 (1999).

6   H. Takagi, G. Kano, and I. Teramoto, IEEE Transactions on Electron Devices **25** (5), 551 (1978).

7   C. J. Huang, Z. S. Ya, J. H. Horng, M. P. Houng, and Y. H. Wang, Japanese Journal of Applied Physics Part 1-Regular Papers Short Notes & Review Papers **41** (9), 5561 (2002).

8   A. Colquhoun, E. Kohn, and H. L. Hartnagel, IEEE Transactions on Electron Devices **25** (3), 375 (1978).

9   K. Rajagopalan, J. Abrokwah, R. Droopad, and M. Passlack, IEEE Electron Device Letters **27** (12), 959 (2006).

10   K. Rajagopalan, R. Droopad, J. Abrokwah, P. Zurcher, P. Fejes, and M. Passlack, IEEE Electron Device Letters **28** (2), 100 (2007).

[11]   Y. Taur and T. H. Ning, *Fundamentals of Modern VSLI Devices*. (Cambridge University Press, Melbourne, 1998).

[12]   J. A. Stroscio, R. M. Feenstra, and A. P. Fein, Physical Review Letters **58** (16), 1668 (1987).

[13]   J. A. Stroscio, R. M. Feenstra, and A. P. Fein, Physical Review B **36** (14), 7718 (1987).

[14]   C. Kittel, (John Wiley & Sons, Inc., Hoboken, 1996).

[15]   S. K. Tewksbury, *Semiconductor Materials*. (1995).

[16]   G. Eftekhari, Thin Solid Films **257** (1), 110 (1995).

[17]   J. L. Freeouf, D. A. Bachanan, S. L. Wright, T. N. Jackson, and B. Robinson, Applied Physics Letters **57** (18), 1919 (1990).

[18]   D. Sengupta and V. Kumar, Physica Status Solidi a-Applied Research **73** (2), K279 (1982).

[19]   H. Becke, R. Hall, and J. White, Solid-State Electronics **8**, 813 (1965).

[20]   E. Kohn and A. Colquhoun, Electronics Letters **13** (3), 73 (1977).

[21]   R. K. Ahrenkiel and D. J. Dunlavy, Solid-State Electronics **27** (5), 485 (1984).

[22]   M. Hong, M. Passlack, J. P. Mannaerts, J. Kwo, S. N. G. Chu, N. Moriya, S. Y. Hou, and V. J. Fratello, Journal of Vacuum Science & Technology B **14** (3), 2297 (1996).

[23]   M. Passlack, M. Hong, J. P. Mannaerts, J. R. Kwo, and L. W. Tu, Applied Physics Letters **68** (25), 3605 (1996).

[24]   T. T. Chiang and W. E. Spicer, Journal of Vacuum Science & Technology a-Vacuum Surfaces and Films **7** (3), 724 (1989).

[25]   J. L. Freeouf and J. M. Woodall, Applied Physics Letters **39** (9), 727 (1981).

[26]   E. R. Weber, H. Ennen, U. Kaufmann, J. Windscheif, J. Schneider, and T. Wosinski, Journal of Applied Physics **53** (9), 6140 (1982).

[27]   R. E. Allen and J. D. Dow, Journal of Vacuum Science & Technology **19** (3), 383 (1981).

[28]   W. E. Spicer, Z. Lilientalweber, E. Weber, N. Newman, T. Kendelewicz, R. Cao, C. Mccants, P. Mahowald, K. Miyano, and I. Lindau, Journal of Vacuum Science & Technology B **6** (4), 1245 (1988).

[29]   M. J. Hale, J. Z. Sexton, D. L. Winn, A. C. Kummel, M. Erbudak, and M. Passlack, Journal of Chemical Physics **120** (12), 5745 (2004).

[30]   M. J. Hale, S. I. Yi, J. Z. Sexton, A. C. Kummel, and M. Passlack, Journal of Chemical Physics **119** (13), 6719 (2003).

[31]   N. Negoro, H. Fujikura, and H. Hasegawa, Applied Surface Science **159**, 292 (2000).

[32]   R. C. Blanchet and B. J. Delhomme, Vacuum **32** (1), 3 (1982).

[33]   J. G. Tenedorio and P. A. Terzian, Ieee Electron Device Letters **5** (6), 199 (1984).

[34]   A. Paccagnella, E. Zanoni, C. Tedesco, C. Lanzieri, and A. Cetronio, IEEE Transactions on Electron Devices **38** (12), 2682 (1991).

35   G. J. Gerardi, F. C. Rong, E. H. Poindexter, M. Harmatz, H. Shen, and W. L. Warren, Colloids and Surfaces a-Physicochemical and Engineering Aspects **72**, 161 (1993).

36   See EPAPS Document No. E-JCPSA6-126-707641 for decap procedure example. This document can be reached through a direct link in the online article's HTML reference section or via EPAPS homepage (http://www.aip.org/pubservs/epaps.html).

37   P. Martensson and R. M. Feenstra, Physical Review B **39** (11), 7744 (1989).

38   R. M. Feenstra, Physical Review B **50** (7), 4561 (1994).

39   R. M. Feenstra and J. A. Stroscio, Journal of Vacuum Science & Technology B **5** (4), 923 (1987).

40   J. Behrend, M. Wassermeier, L. Daweritz, and K. H. Ploog, Surface Science **342** (1-3), 63 (1995).

41   Q. K. Xue, T. Hashizume, and T. Sakurai, Applied Surface Science **141** (3-4), 244 (1999).

42   J. E. Northrup and S. Froyen, Physical Review B **50** (3), 2015 (1994).

43   W. G. Schmidt and F. Bechstedt, Physical Review B **54** (23), 16742 (1996).

44   T. Hashizume, Q. K. Xue, J. Zhou, A. Ichimiya, and T. Sakurai, Physical Review Letters **73** (16), 2208 (1994).

45   I. Chizhov, G. Lee, R. F. Willis, D. Lubyshev, and D. L. Miller, Surface Science **419** (1), 1 (1998).

46   N. Moll, A. Kley, E. Pehlke, and M. Scheffler, Physical Review B **54** (12), 8844 (1996).

47   V. P. LaBella, H. Yang, D. W. Bullock, P. M. Thibado, P. Kratzer, and M. Scheffler, Physical Review Letters **83** (15), 2989 (1999).

48   J. A. Stroscio, R. M. Feenstra, and A. P. Fein, Physical Review B **36**, 7718 (1987).

49   J. A. Stroscio and R. M. Feenstra, Journal of Vacuum Science Technology A **6**, 577 (1988).

50   M. D. Pashley, Physical Review B **40** (15), 10481 (1989).

51   G. Kresse and J. Furthmüller, Computational Materials Science **6** (1), 15 (1996).

52   G. Kresse and J. Furthmüller, Physical Review B **54** (16), 11169 (1996).

53   G. Kresse and J. Hafner, Physical Review B **47** (1), 558 (1993).

54   G. Kresse, Technische University at Wien, 1993.

55   J. P. Perdew, K. Burke, and M. Ernzerhof, Physical Review Letters **77** (18), 3865 (1996).

56   P. E. Blochl, Physical Review B **50** (24), 17953 (1994).

57   G. Kresse and D. Joubert, Physical Review B **59** (3), 1758 (1999).

58   H. J. Monkhorst and J. D. Pack, Physical Review B **13**, 5188 (1976).

59   J. Paier, R. Hirschl, M. Marsman, and G. Kresse, Journal of Chemical Physics **122** (23) (2005).

60   N. Lorente, M. F. G. Hedouin, R. E. Palmer, and M. Persson, Physical Review B **68** (15) (2003).

61   K. Seino, W. G. Schmidt, M. Preuss, and F. Bechstedt, Journal of Physical Chemistry B **107** (21), 5031 (2003).

62   G. Henkelman, A. Arnaldsson, and H. Jonsson, Computational Materials Science **36** (3), 354 (2006).

63   G. X. Qian, R. M. Martin, and D. J. Chadi, Physical Review B **38** (11), 7649 (1988).

64   C. G. Van de Walle and J. Neugebauer, Physical Review Letters **88** (6) (2002).

65   J. Tersoff and H. D.R., Physcal Review B **31**, 805 (1985).

66   *Handbook of Chemistry and Physics*, 85 ed. (CRC Press, Boca Raton, 2004).

67   P. Kruse, J. G. McLean, and A. C. Kummel, Journal of Chemical Physics **113** (20), 9224 (2000).

68   D. L. Winn, M. J. Hale, T. J. Grassman, A. C. Kummel, R. Droopad, and M. Passlack, Journal of Chemical Physics **126** (8) (2007).

69   G. Kresse and J. Hafner, Journal of Physics: Condensed Matter **6** (40), 8245 (1994).

70   *Handbook of Chemistry and Physics*, 87 ed. (CRC Press, Boca Raton, 2006).

71   R. M. Feenstra, J. A. Stroscio, and A. P. Fein, Surface Science **181** (1-2), 295 (1987).

72   R. Maboudian, K. Pond, V. Bresslerhill, M. Wassermeier, P. M. Petroff, G. A. D. Briggs, and W. H. Weinberg, Surface Science **275** (1-2), L662 (1992).

[73]   W. G. Schmidt, Applied Physics a-Materials Science & Processing **75** (1), 89 (2002).

[74]   R. H. Miwa, R. Miotto, and A. C. Ferraz, Surface Science **542** (1-2), 101 (2003).

[75]   Q. K. Xue, Y. Hasegawa, T. Ogino, H. Kiyama, and T. Sakurai, Science Reports of the Research Institutes Tohoku University Series a-Physics Chemistry and Metallurgy **44** (2), 153 (1997).

[76]   C. Ratsch, W. Barvosa-Carter, F. Grosse, J. H. G. Owen, and J. J. Zinck, Physical Review B **62** (12), R7719 (2000).

[77]   C. Kendrick, G. LeLay, and A. Kahn, Physical Review B **54** (24), 17877 (1996).

[78]   S. Ohkouchi and N. Ikoma, Japanese Journal of Applied Physics Part 1-Regular Papers Short Notes & Review Papers **33** (6B), 3710 (1994).

[79]   S. M. Lee, S. H. Lee, and M. Scheffler, Physical Review B **69** (12) (2004).

[80]   J. G. McLean, P. Kruse, G. P. Jiang, H. E. Ruda, and A. C. Kummel, Physical Review Letters **89** (23) (2002).

[81]   C. B. DeMelo, D. C. Hall, G. L. Snider, D. Xu, G. Kramer, and N. El-Zein, Electronics Letters **36** (1), 84 (2000).

[82]   J. M. Millunchick, A. Riposan, B. Dall, C. Pearson, and B. G. Orr, Surface Science **550** (1-3), 1 (2004).

[83]   L. Li, B. K. Han, R. F. Hicks, H. Yoon, and M. S. Goorsky, Ultramicroscopy **73** (1-4), 229 (1998).

84   J. M. Millunchick, A. Riposan, B. J. Dall, C. Pearson, and B. G. Orr, Applied Physics Letters **83** (7), 1361 (2003).

85   A. Chakrabarti, P. Kratzer, and M. Scheffler, Physical Review B **74** (24) (2006).

86   A. Chakrabarti and K. Kunc, Physical Review B **68** (4) (2003).

87   A. Chakrabarti and K. Kunc, Physical Review B **70** (8) (2004).

88   J. H. Cho, S. B. Zhang, and A. Zunger, Physical Review Letters **84** (16), 3654 (2000).

89   P. Kratzer, E. Penev, and M. Scheffler, Applied Surface Science **216** (1-4), 436 (2003).

90   E. Penev, S. Stojkovic, P. Kratzer, and M. Scheffler, Physical Review B **69** (11) (2004).

91   D. Vanderbilt, Physical Review B **41** (11), 7892 (1990).

92   J. M. Moison, C. Guille, F. Houzay, F. Barthe, and M. Vanrompay, Physical Review B **40** (9), 6149 (1989).

93   D. L. Winn, M. J. Hale, T. J. Grassman, J. Z. Sexton, A. C. Kummel, R. Droopad, and M. Passlack, Journal of Chemical Physics (Submitted).